IJAPLett

IRAQI JOURNAL OF APPLIED PHYSICS LETTERS

IJAPLett

Iraqi Journal of Applied Physics (IJAPLett) is a scientific periodical sponsored and published by the Iraqi Society for Alternative and Renewable Energy Sources and Techniques (I.S.A.R.E.S.T.). The Editorial Board is responsible for the scientific content and other editorial matters relating to the Journal. Manuscripts submitted are first screened by the editors; those on subject matters within the scope of the **IJAPLett** are sent to an expert referee for evaluation and may be sent to a second reviewer if necessary. This screening process helps to assure an appropriate focus as well as high scientific quality of the Journal. The **IJAPLett** welcomes submission of papers and letters in applied physics and related fields of science, engineering and technology. They should have something in common with what we now publish on inanimate materials and processes therein: structures, transport, physical, electrical, dielectric, magnetic, and optical properties. Our basic criterion stated below will continue to apply: papers must contain science, especially physics, and there must be an application. We advise authors submitting papers to suggest the names of at least two possible reviewers, with full information on addresses, phone and e-mail. Suggestions of reviewers are welcome regardless of the subject.

AIMS AND SCOPES

Alternative & Renewable Energy
Applied Mechanics & Thermodynamics
Applied Optics & Optical Design
Biophysics & Bioengineering
Cryptography & Applications
Electromagnetic Fields
Electronic Materials & Devices
Energy Generation & Conversion
Fluids Physics & Mechanics
Imaging, Microscopy & Spectroscopy
Laser Physics & Applications
Magnetism & Applications
Instrumentation, Measurements & Metrology
Nanostructures & Applications
Nonlinear & Ultrafast Optics
Nuclear Physics & Engineering
Optical Communications & Systems
Optoelectronics Devices & Applications
Organic Materials, Devices & Applications
Physical Chemistry & Biochemistry
Plasma, Discharge Physics & Applications
Quantum Physics & Spectroscopy
RF & Digital Communications
Semiconductors & Devices
Simulation & Modeling Research
Solar Energy & Devices
Solid State Physics & Applications
Structure & Properties of Matter
Superconductivity & Related Devices
Surfaces, Interfaces & Films
Thin Films & Applications
Vacuum Science & Technology

SPONSORED AND PUBLISHED BY

THE IRAQI SOCIETY FOR ALTERNATIVE AND RENEWABLE ENERGY SOURCES AND TECHNIQUES (I.S.A.R.E.S.T.)

PRINTED IN IRAQ

ISSN 1999-656X

EDITORIAL BOARD

" INSTRUCTIONS TO AUTHORS "

CONTRIBUTIONS

Contributions to be published in this journal should be original research works, i.e., those not already published or submitted for publication elsewhere, individual papers or letters to editor.

SUBMISSION OF MANUSCRIPTS

Manuscripts should be submitted to one of the following addresses:

Iraqi Journal of Applied Physics Letters
Dr. Raad Azzawi KHAMIS
Editor-in-Chief
Branch of Laser & Optoelectronics,
School of Applied Sciences,
University of Technology,
P. O. Box 35010,
Baghdad, IRAQ

Iraqi Journal of Applied Physics Letters
Oday Ata HAMADI
Managing Editor
P. O. Box 55259,
Baghdad 12001, IRAQ
Tel.: +964-7901274190
Tel.: +964-7702523071
Email: ijaplett.editor@hotmail.com

MANUSCRIPTS

Two copies with soft copy on a compact disc (CD) should be submitted to Editor in the following configuration:

- Double-spaced one-side A4 size with 2.5 cm margins of all sides
- 12pt Times New Roman font
- Letters should not exceed 12 pages.
- Manuscripts presented in English only are accepted.
- Authors confirm affiliations, addresses and emails. Email is necessary for correspondences. The corresponding author will be assigned by asterisk (star sign) to refer to its corresponding address.
- English abstract not exceed 150 words
- 4 keywords (at least) should be maintained on (PACS preferred)
- Author(s) should express all quantities in SI units
- Equations should be written in equation form (italic and symbolic)
- Figures and Tables should be separated from text
- Figures and diagrams can be submitted in colors for assessment and they will be returned to authors after provide printable copies
- Charts should be indicated by the software used for
- Only original or high-resolution scanner photos are accepted
- References are written in titles, full-name authors, names of publications, years, volumes, issues and pages (from-to)

PROOFS

Authors will receive proofs of papers and are requested to return one corrected hard copy with a WORD copy on a compact disc (CD). New materials inserted in the original text without Editor permission may cause rejection of paper.

COPYRIGHT FORM

Author(s) will be asked to transfer copyrights of the article to the Journal soon after acceptance of it. This will ensure the widest possible dissemination of information.

OFFPRINTS

Authors will receive offprints free of charge and any additional offprints can be ordered.

SUBSCRIPTION AND ORDERS

Annual fees (4 issues per year) of subscription are:

- 50 000 Iraqi dinars for individuals and establishments inside Iraq.
- 50 US$ for individuals and establishments abroad.

Orders of issues can be submitted by contacting the editor-in-chief or editorial secretary to maintain the address of issue delivery and payment way.

Ali M. Mousa
Adawiya J. Haider*
Ahmed S. Jabbar

School of Applied Sciences,
University of Technology,
Baghdad, IRAQ
** adawiya_haider@yahoo.com*

Characterization of D.C. Sputtering System

DC sputtering system was designed and fabricated and it used for deposition cadmium films. The optimum conditions for deposition was determined experimentally under different voltages, pressures, and inter - electrode distances. XRD spectrums show a clear indication of (hcp) peaks which belongs to pure cadmium metal.

Keywords: DC sputtering, cadmium thin film, XRD, Electrical Characterization
Received: 20 April 2008, Accepted: 20 May 2008

1. Introduction

Sputtering process has been used as a tool for depositing thin films and coating after discovering it in 1852 by W.R. Grove. [1]. We can describe the sputtering process by formation of plasma due to electric discharge with sputtering gas which pumped under a certain pressure to deposition chamber previously evacuated to less than 10^{-6}Torr [2]. Voltage is applied to start glow discharge and sputtering. Generated positive ions will bombard target (cathode) and sputter target's material on substrate (anode), while the negative electrons and secondary electrons are accelerated due to electric field to maintain ionization by much more of ionization collisions with gas medium.

If kinetic energy of bombarding ion is larger than cohesive energy of target's material, which related to sublimation energy of target's material, then bombarding will lead to atomic displacement to new positions and therefore, result in form of surface migration and then surface damage. If kinetic energy being much more than (4H) (Where H is heat of sublimation), the ejecting and sputtering atoms to gas medium is the permanent effect under ion bombardment [1].

There are many theories used to explain the mechanism of sputtering process such as momentum transfer, hot spot evaporation and radiation damage theories, but the first one is much acceptable within sputtering field [6].

2. Experimental Design and Construction

The cathode has been designed from copper into two pieces, first was in form of disc with external diameter of 80mm and thickness of 11mm and contains a central cylindrical cavity with diameter of 51mm and depth of 5mm used for fixing sputtering target. This disc is supported on a copper cylinder of 80mm diameter and 42mm height.

The anode was made of rectangular stainless steel plate with dimensions of (100x45x1)mm. Substrate with dimensions of (76x25x1)mm are fixed on anode after masking them using aluminium masks of a certain uniform shapes. The lower cylinder contains a cylindrical cavity of 40mm diameter and 36mm height used as a water sink to cool cathode, which supplied by a copper pipe welded in the base of the lower cylinder. The cathode (copper disc and lower cylinder) was covered with aluminum shield (except surface of target) to prevent the sputtering from undesired part of cathode. The distance between this shield and the outer cathode surface was 4mm.

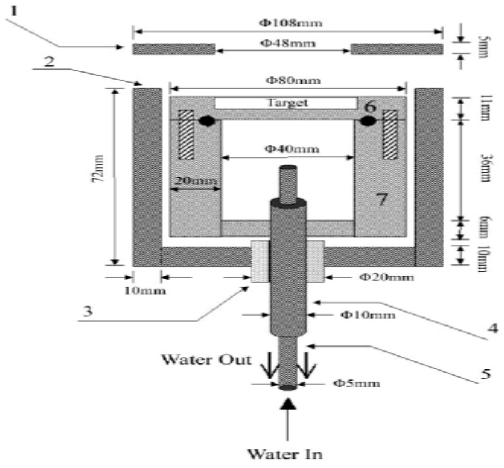

Fig. (1) Geometrical scheme of fabricated cathode

To prevent the accommodation of thermal evaporation and atomic rediffusion within target's material (in case of multi-components target), the cathode was cooled by 15°C water supplied by a pair of coaxial copper pipes that welded with the lower base of cylinder. These pipes were isolated from aluminum shield using a small cylinder piece of Teflon. Fig. (2) shows the upper view of the cathode assembly.

For reducing feed-through in the system, then to prevent any leakage during operating of system, we used the cooling coaxial pipes as a high voltage connector. Therefore, we isolated them from the chamber base using a Teflon pipe

of 80mm length and 20mm diameter. This pipe was also covered by aluminum pipe of 60mm length and 28mm diameter containing at one end a flange matching with the flange of pipe-chamber base.

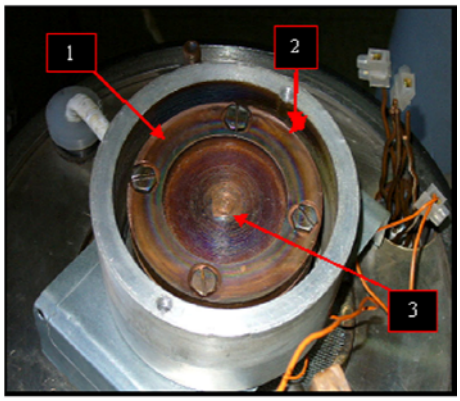

Fig. (2) Upper view of fabricated cathode assembly. (1) The cathode (2) The space between cathode and Aluminum shield (3) Target position

The reason for using copper and aluminum metals in our design is the availability of these metals and feasibility in operation to get the desired designs, as well as their good thermal and electrical conductivities. The slides were cleaned using pure ethanol (99.9%) with ultrasonic bath (T-7, L&R) to remove all contaminations on their surfaces.

Vacuum unit consists of two pumps: the first is a mechanical-rotary pump and the second is an oil-diffusion pump. Sputtering gas unit consists of argon gas cylinder of (99.999%) purity. Cadmium of (99.999%) purity provided by (Leybold-Heraeus-GmbH) in form of 4mm-diameter grains has been used as target, because it has a higher sputtering yield coefficient than the other elements due to its low cohesive energy [8].

Prior to sputtering, the chamber was pumped down to a base pressure of 10^{-4}Torr in order to avoid the contaminations, then flushed with pure argon several times in order to remove very small amounts of the residual gases further.

Cadmium grains were pressed using a hydraulic press (DIN) and a stainless steel mold under 12tons for 12min to obtain a disc of 50mm diameter and 6mm thickness. The surface of target was polished using 320um and 500um papers and washed with ethyl alcohol of (99.9%) purity. A DC power supply was fabricated to provide high voltage extended to 30kV.

X-ray diffraction test was performed for the sputtered films and ASTM standardizations were used for comparison with measured relative X-ray intensities of deposited films to determine their crystal planes. Interplanar distance (*d*) of thin films was calculated using the Bragg's diffraction equation and the film thickness was measured by optical interference fringes method using a 632.8nm He-Ne laser.

3. Results and Discussion

A. Structural Study

The sputtered films deposited at different conditions have polycrystalline structures as shown by XRD peaks that exhibit the hexagonal closed packed (*hcp*) which belongs to pure cadmium metal. Fig. (3) shows the diffraction spectra of deposited films.

Fig. (3a) shows the XRD of a film deposited at 4.4kV, 0.08Torr and 2cm at 100°C. The thickness of this film (2531Å), which exhibits a preferential orientation of (101) plane appears at 2θ=38.4º. Fig. (3b) belonging to a film of 3164Å thickness exhibits the plane (101) at 2θ=38.4º too but at condition of at 4.6kV, 0.08Torr and 2cm at 134°C. As for plane (101), Fig. (3c) exhibits a plane (103) at 2θ=59.6º, which belongs to a film deposited at 4.6kV, 0.08Torr and 2cm at 130°C. The thickness of this film was 3059Å. While Fig. (3d) shows a diffraction peak belongs to CdO structure at plane (111) at diffraction angle of 2θ=33.1º, which belongs to film sputtered at 4.6kV, 0.08Torr and 3cm at 130°C, just like to (101) plane belonging to pure cadmium. This oxide is arising due to oxidation of films. All sputtering process were performed for 30min.

B. Electrical Characterization

Fig. (4) shows the variation of sputtering yield coefficient with applied voltage. The applied voltage in the region (1) was below down to 3.5kV, and we performed many depositions processes at these energies for 30min. These processes did not give us any value of sputtering yield coefficient due to very small numbers of sputtered atoms.

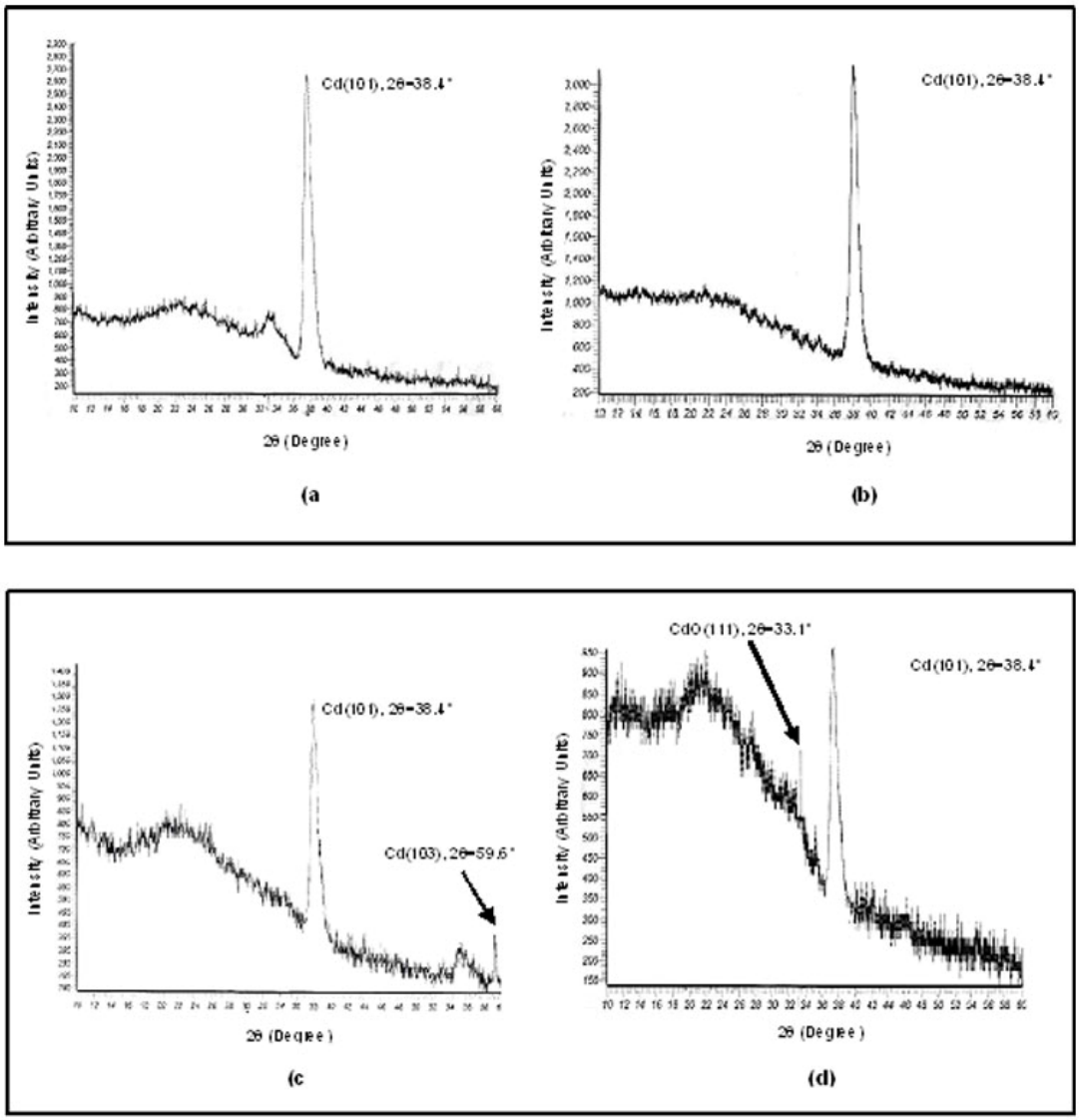

Fig. (3) XRD spectra of sputtered films at different deposition conditions (a) at 4.4kV, 0.08Torr, and 2cm (b) at 4.6kV, 0.08Torr, and 2cm (c) at 4.6kV, 0.08Torr, and 2cm (d) at 4.6kV, 0.08Torr, and 3cm

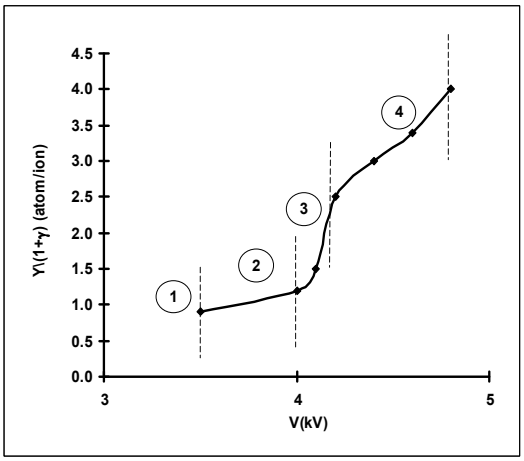

Fig. (4) Sputtering yield coefficient vs. applied voltage. p=0.08Torr, d=2cm and time=30min

The region (2) is extended from 3.5kV to 4kV, which is characterized by increasing sputtering yield coefficient at slow rate with increasing applied voltage. This is due to the low kinetic of positive ion, which bombarded target. So, the transferred momentum to surface atoms is small. So, the sputtering of atoms is done under many collisions of positive ions with target as can be shown in Fig. (5), which shows increasing discharge current with increasing applied voltage.

The region (3) is extended from 4kV to 4.4kV, which is characterized by fast increment rate of sputtering yield coefficient with applied voltage as compared with the second region. This is due to increasing applied voltage as shown in Fig. (4), where the increment of positive ions contribute firstly in increment of number of positive ions, and secondly increasing its kinetic energy.

The region (4) is extended from 4.4kV to 4.8kV and characterized by continuous increment of sputtering yield coefficient with increasing applied voltage, but at a slower rate

than in the third region. This is due increasing number of collisions between positive ions and plasma particles, which lead to decrease the kinetic energy of positive ions and change their paths to many directions far away of target. This behavior affects negatively on the sputtering yield coefficient. The obtained results in former last regions matched with results obtained for copper, silver, and cadmium targets [6].

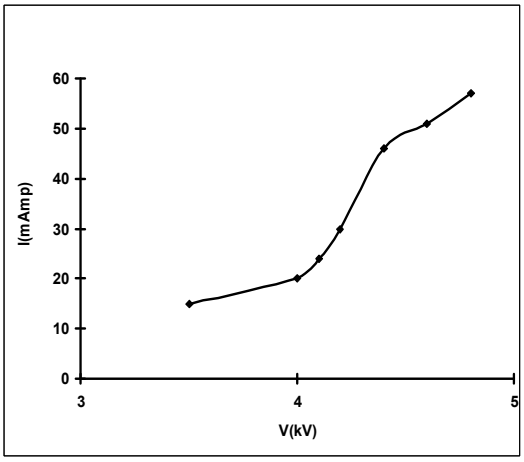

Fig. (5) Discharge current vs. applied voltage. p=0.08Torr, d=2cm and time=30 min

Fig. (6) shows the increasing of sputtering yield coefficient with increasing deposition pressure within (0.03-0.3)Torr. This is due to increasing generated positive ion density within deposition medium at increasing deposition pressure, because the number of generated ions is proportional to gas pressure. This will lead to increase efficiency of ions bombardment to target's surface.

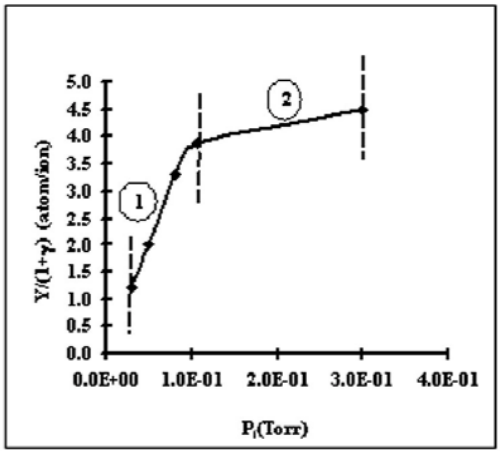

Fig. (6) Sputtering yield coefficient vs. deposition pressure. V=4.6kV, d=2cm and time=30min

Fig. (7) shows the increment in discharge current with deposition, where this increment shows the dependence of the sputtering yield coefficient on discharge current (density of generated ions). The region (1) is extended from 0.03Torr to 0.1Torr and characterized by fast increment sputtering yield coefficient, which belongs to increasing of positive ion density with increasing of deposition pressure at constant voltage, as well as increasing of kinetic energy of these ions. This enhanced the efficiency of ion bombardment of target. This can be noticed from increment of discharge current in the pressure range (0.03-0.3)Torr, as illustrated in Fig. (7).

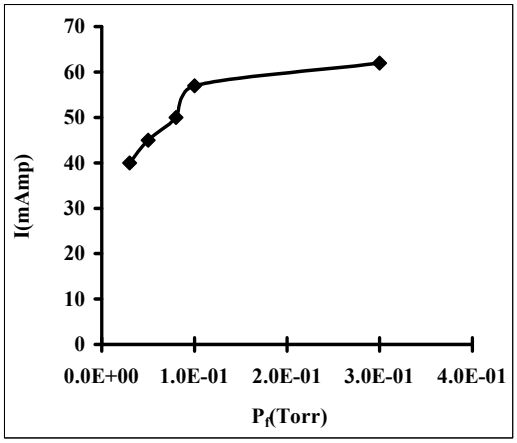

Fig. (7) Discharge current vs. deposition pressure. V=4.6kV, d=2cm and time=30min

The region (2) is extended from 0.1Torr to 0.3Torr and characterized by continuous increment of sputtering yield coefficient with increasing deposition pressure but at a slower rate than obtained in first region. This behavior can be explained according to increasing the density of generated ions in sputtering plasma, which will lead to reduce the mean free path of the bombarding ions to the target's surface. Therefore, this will reduce their kinetic energy and change their paths to different direction far away of target's surface, which will affect negatively on the value of the sputtering yield coefficient in case of incrementing deposition pressure.

From Fig. (8), which shows the variation of sputtering yield coefficient with inter-electrode distance, we note a decrement in sputtering yield coefficient due to decrementing kinetic energy of accelerated ions under certain electric field. The increment inter-electrode distance lead to increase the number of ionized collisions between electrons and gas atoms which will lead to increase discharge current as shown in Fig.(9). Therefore, this will lead to reduce the mean free path of accelerated positive ions to target, which affects negatively on the value of sputtering yield coefficient.

Fig. (10) shows the variation of film deposition rate under different applied voltages. The region (1) is extended from 3.5kV to 4.1kV and characterized by increasing the deposition rate with increasing applied voltage at a very slow rate, which belongs to collisions happened by sputtered atoms during their paths to substrate. These collisions reduce the kinetic

energies of sputtered atoms and change their paths far away of substrate. This effect is shown by means of changes in substrate temperature (T_s) with applied voltage as shown in Fig.(11), which shows the kinetic energies of sputtered ions arriving to the substrate.

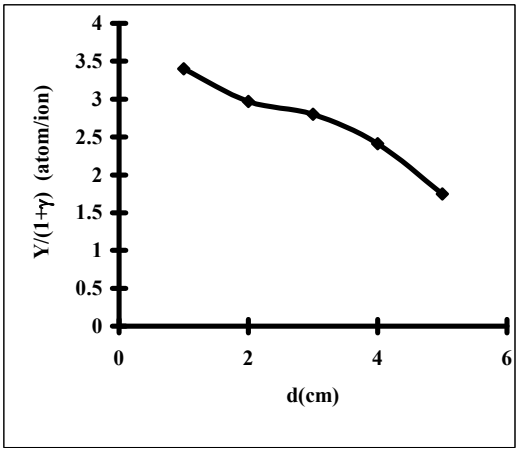

Fig. (8) Sputtering yield coefficient vs. Inter-electrode distance. V=4.6kV, p=0.08Torr and time=30min

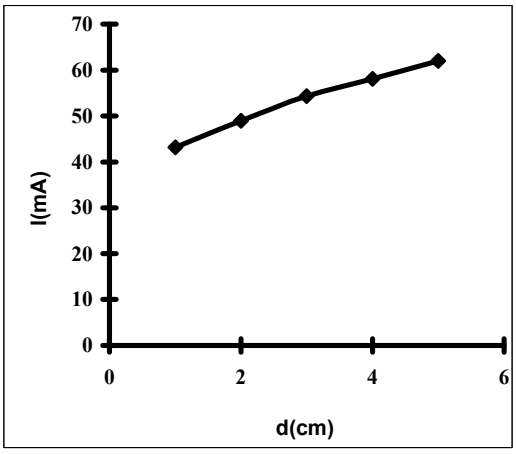

Fig. (9) Discharge current vs. inter-electrode distance. V=4.6kV, p=0.08Torr and time=30min

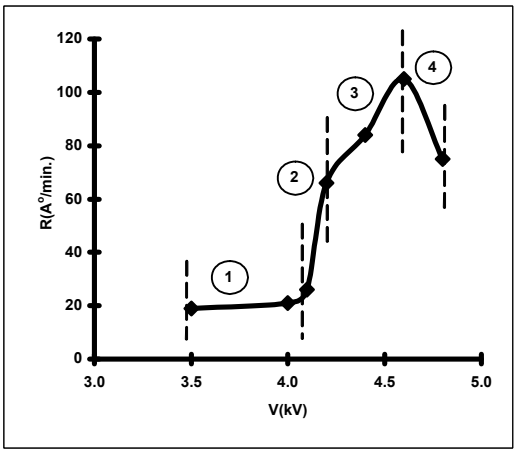

Fig. (10) Deposition rate vs. applied voltage. p=0.08Torr, d=2cm and time=30min

Fig. (11) shows the variation of substrate temperature versus deposition voltage, which is due to incrementing number and energy of generated ions, the incrementing ion bombardment efficiency to target's surface. This leads to eject atoms from surface and condensed them on substrate. Because of transferring the kinetic energy of bombarded ions to surface atoms, so these atoms arrive to substrate at high kinetic energies make them heating substrate, as well as to effect of heating caused by generated secondary electrons within plasma. Therefore, we can depend on substrate temperature as rough indicator to kinetic energy of condensed atoms.

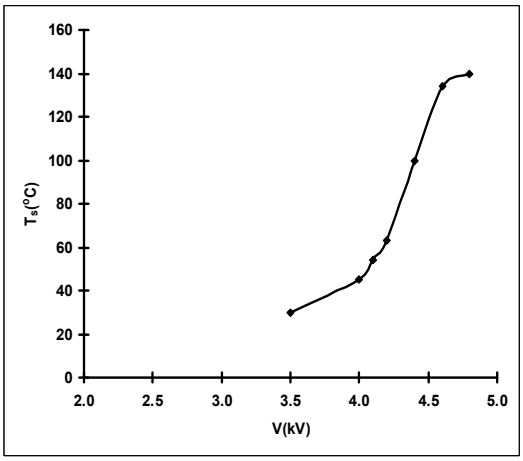

Fig. (11) Substrate temperature vs. deposition voltage. p=0.08Torr, d=2cm and time=30min

The region (2) is extended from 4.1kV to 4.2kV and characterized by fast incrementing deposition rate compared to what found in the first region with increasing of applied voltage. This can be explained according to the increment of generated ion number (increment of discharge current as shown in Fig. (5)), and incrementing energy of bombarding ions to target's surface, which will lead to increase the efficiency of sputtering deposition (as shown in Fig. (4)).

The increment of bombarding ion energy will contribute in increasing of number of sputtered atoms, which most of them will condense on substrate. Then will lead to heat it because of high kinetic energies of condensed atoms which rearranged themselves by action of high surface mobility of these atoms, that will lead to fast heating of substrate, as shown in Fig. (11).

The region (3) is extended from 4.2kV to 4.6kV and characterized by continuous increment in deposition rate with increasing applied voltage, but slower than obtained in the second region. This can be explained due to increasing the plasma density, and consequently increasing number of collisions between sputtered atoms and particles of plasma medium. This will lead to change the paths of some of these atoms far away of substrate. This will affect negatively at a certain ratio on the value of deposition rate.

Generally, we get increment in deposition rate constituting with increasing of applied

voltage to the maximum deposition rate (105Å/min.) at 4.6kV. Our obtained results at the first, second, and third regions match with those found by Risk [13] and Szczyrbowski [14] for copper and InAs, respectively. When we increased the applied voltage over 4.6kV, we noticed a decrement in deposition rate, which would continue with increasing voltage. This is due to increasing generated ion number within sputtering medium with increasing applied voltage that will lead to increase number of collisions performed between plasma particles and sputtered atoms. Again, this will lead to change the paths of some of these atoms, as well as heat the substrate (due to increment of generated positive ions numbers with increasing applied voltage, as shown in Fig. (5)). In addition, these collisions can lead to re-sputter atoms of substrate towards sputtering medium that affect negatively on deposition rate in this region.

Fig. (12) shows the deposition rate variation versus deposition pressure. The region (1) is extended from 0.03Torr to 0.08Torr and characterized by increasing deposition rate with increasing deposition pressure. This is due to the increasing number of generated ions within deposition plasma at increment deposition pressure, which can be noted in increasing discharge current with increasing deposition pressure, as shown in Fig. (7).

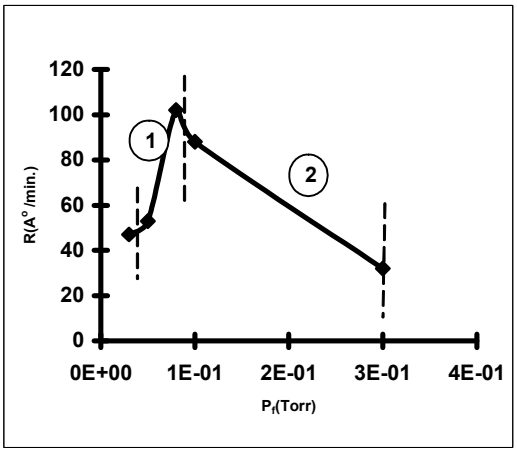

Fig. (12) Deposition rate vs. deposition pressure. V=4.6kV, d=2cm and time=30min

Therefore, the increasing number of generated ions leads to increase the efficiency of ion bombardment to target's surface, thus increasing film deposition rate reaches the maximum (102Å/min) at 0.08Torr. The region (2) is extended from 0.08Torr to 0.3Torr and characterized by decreasing deposition rate at deposition pressure above 0.08Torr due to largely increasing the ion density compared to what obtained in the first region. This behavior leads to perform many collisions between sputtered atoms and plasma particles, then change paths of large ratio of sputtered atoms far away from the substrate.

However, the electronic bombardment to substrate contributes in heating substrate to higher temperature (as well as to affect kinetic energy of condensed atoms), as shown in Fig. (13). This contributes in re-sputtering of condensed atoms on substrate to deposition medium. This affects negatively on the value of deposition rate in this region.

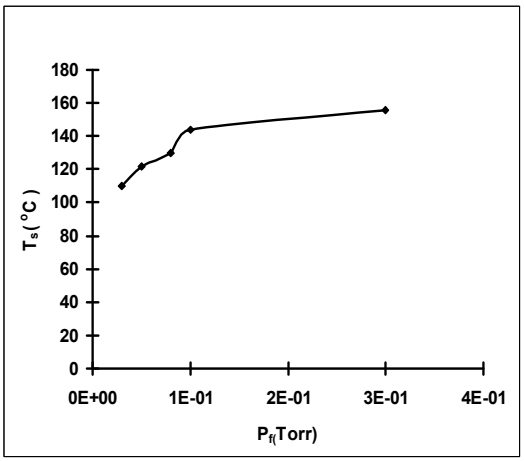

Fig. (13) Substrate temperature vs. deposition pressure. V=4.6kV, d=2cm and time=30min

Fig. (14) shows the variation in deposition rate versus changing inter-electrode distance (between target and substrate). For good explanation, we divided this curve into three main regions: the region (1) is extended from 1cm to 2cm and characterized by increasing deposition rate with increasing inter-electrode distance. This is due to gathering a large number of sputtered atoms thereby substrate. These sputtered atoms arrive far away target's surface and in a random directions with different kinetic energies. Therefore, it is preferred to place the substrate closer to target to collect large ratio of sputtered atoms and deposit them on substrate [4]. This will lead to increase the deposition rate of sputtered films, larger (target diameter/inter-electrode distance) ratio, larger deposition rate and better film uniformity [1]. This behavior matches to what found by Westwood [14].

The region (2) is extended from 2cm to 3cm. In this region, we noted a decrement in deposition rate due to increasing number of collisions between sputtered atoms with plasma particles due to increasing of inter-electrode distance. This means increasing of collisions probability and hence a ratio of these atoms deflect far away of the substrate, so decreasing of deposition rate. This result matches with the results obtained by Risk [13] and Westwood [14].

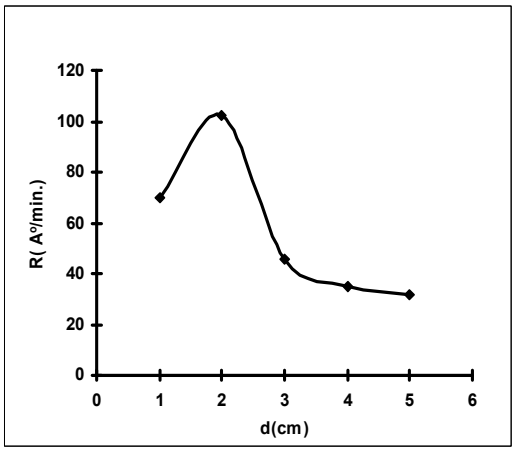

Fig. (14) Deposition rate vs. inter-electrode distance. V=4.6 kV, p=0.08Torr and time=30min

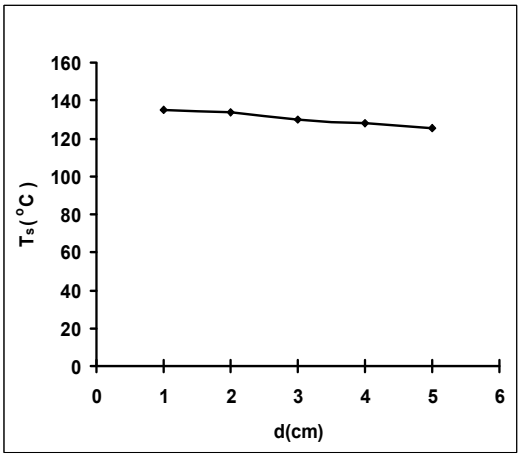

Fig. (15) Substrate temperature vs. inter-electrode distance. V=4.6 kV, p=0.08Torr and time=30min

The region (3) is extended from 3cm to 5cm and characterized by continuing decrement in deposition rate with increasing inter-electrode distance, but at a slower rate than what found in the second region due to decrement in number of arrival sputtered atoms to substrate.

4. Conclusions

In this work, we successfully designed and fabricated a d.c. sputtering system and tested it under different deposition conditions including voltage, pressure, and inter-electrode distance to deposit cadmium thin films. XRD study shows polycrystalline structure of deposited films with preferred orientation at (101) plane. Sputtering yield exhibits clear increment with increasing applied voltage and deposition pressure, but it shows clear decrement with increasing the inter-electrode distance. The obtained deposition rate shows a distinct increment with increasing applied voltage, deposition pressure, and inter-electrode distance.

References

[1] L.I. Maissel and R. Glang, **"Handbook of Thin Film Technology"**, McGraw-Hill Book Company, New York,(1970).

[2] B.N. Chapman, **"Glow Discharge Processes"**, John-Wiley and Sons Company, New York, (1980).

[3] J.L. Vossen and W. Kern, **"Thin Film Processes"**, Academic Press, New York, (1978).

[5] Biltoft, Benafl, and Swain, J. Vac. Technol., 60A and 60B, Las Positas College, (2002).

[6] R. Behrish, *Topics in Appl. Phys. Series*, Vol. 47 (1981).

[7] R. Stuart, **"Vacuum Technology, Thin Films, and Sputtering: An Introduction"**, Academic Press, New York, (1983).

[8] A. Anders, *J. Vacuum*, Vol. 67 (2002).

[9] B.D. Cullity, "**Elements of X-ray Diffraction"**, 2nd ed., Addison-Wesley Publicating Company, Reading, (1978).

[10] M. Hernandez, A. Juarez, and R. Hernandez, *Superficies y Vacio* 9, (1999).

[11] D.A. Gerd and F.J. Bush, **"Principles of Physics"**, 1995.

[12] J. Szczyrbowski, A. Czapla, and M. Jachimowski, *Thin Solid Films*, Vol. 42 (1977).

[13] A. Risk et al., *J. of Vacuum*, Vol.39, No.5/6 (1989).

[14] W.D. Westwood, *J. Vacuum Sci. Technol.*, Vol.15, No.1 (1978).

Oday A. Hamadi [1]
Khawla S. Khashan [2]*

[1]*Department of Laser and Optoelectronics Engineering, University of Technology, Baghdad, IRAQ*
[2]*School of Applied Sciences, University of Technology, Baghdad, IRAQ*
** khawla_salah@yahoo.com*

Modeling of the Preheating Effect on Keyhole Laser Welding Efficiency

In this work, results of a mathematical analysis of the role of workpiece preheating in laser keyhole welding were presented. This analysis considered the steady-state welding as well as certain range of boundary conditions over which preheating effect would be indicated. This work is an attempt to interpret the role of preheating to increase welding depth and perform keyhole welding with high quality using physical and thermal properties of steel alloys.

Keywords: Preheating effect, Keyhole welding, Laser welding, Low-carbon steel
Received: 5 April 2008, Accepted: 25 May 2008

1. Introduction

Welding with high power lasers is commonly used nowadays in modern industries due to high productivity, flexibility and high quality provided by laser in addition to possibility to carry out advanced and complicated welding processes. Compared to the conventional welding techniques, use of CO_2 and Nd:YAG lasers with precise control of laser beam parameters made it possible to control welding depth as well as detect defects inside the structure of welded region. Also, controlling welding depth makes it possible to carry out such processes without any side effects to the welded regions or surroundings [1]. In laser welding, the affected area is small and localized and welding process is usually fast then the distortion is minimal [2].

As the material being irradiated by a high power laser beam, surface temperature rises rapidly if the laser beam intensity is high enough. Hence, laser energy absorbed by material is increased as more energy being accumulated onto small volume at the surface [3-5]. Continuing irradiating, the surface will melt at beam incidence point then vaporize to form a hole through which most of incident laser energy being absorbed. If the welding required is deep then the Gaussian distribution and divergency of laser beam form a key-shape hole so this type of welding is known as "keyhole welding". In this process, the incident laser beam penetrates material surface completely and moves along the path between two samples wanted to weld. The quality of laser keyhole welding depends on samples alignment and width of working region [6]. Fig. (1) explains laser keyhole welding process.

Laser keyhole welding, and whole industrial processes, is based on the fundamentals of heat transfer from power source (laser beam) to the workpiece. Although this process seems an ordinary thermodynamic process between two media different in temperature, the problem of heat transfer in such processes is often complex due to many variables included [7-10]. Good understanding of laser keyhole welding process requires more models describing such process and presents enough data in order to be studied and analyzed. Each of effects of variables included can also be studied individually or together with others in order to control welding process [11-12].

Several previous works included analyses and mathematical models related to the parameters of laser keyhole welding process as well as thermal properties of the material welded by high power focused beams [13-22]. These works were all based on the line source model (LSM) of workpiece temperature distribution relative to the cross section of welded region in addition to effects of latent heat of fusion [15-19]. According to the analyses presented in these works, preheating effect on the parameters of laser keyhole welding process can be studied and discussed.

The laser power penetrating workpiece through the keyhole (P_{KH}) formed on workpiece surface is given as:

$$P_{KH} = \eta_a \eta_{KH} P_B \qquad (1)$$

where η_a and η_{KH} are absorption and keyhole coupling efficiencies, respectively, and P_B is laser beam power. Assuming that laser keyhole welding process is carried out under the steady-state condition, as other parameters are constant, the absorption efficiency (η_a) is determined by the reflectivity of the molten, which in turn depends on the effect of plasma present in beam path toward workpiece [23-25]. This efficiency does not depend on preheating temperature since the region surrounding material-beam interaction

region is already melted that may cause to absorb all the incident power. Preheating affects the absorption efficiency just in non-steady states such as beginning welding process [24].

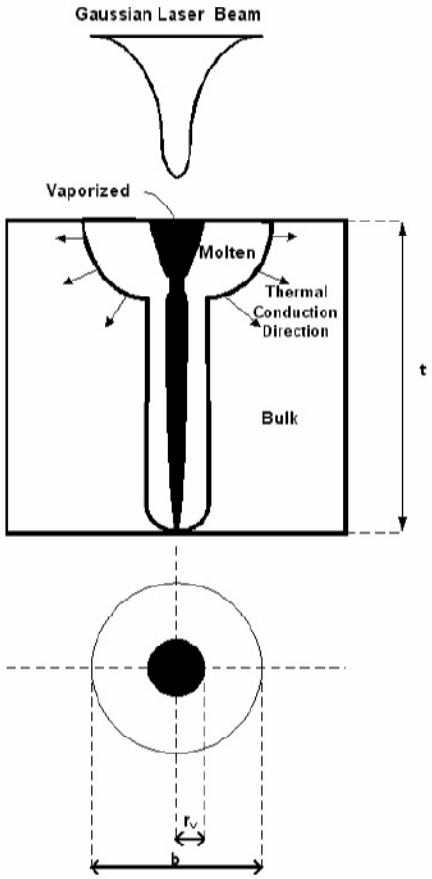

Fig. (1) Principle of laser keyhole welding

The other parameter determining the mount of laser power transferred into workpiece is the efficiency of energy transfer through keyhole (η_{KH}) which represents a function depends precisely on the ratio of keyhole radius on surface (r_v) to incident laser beam radius (r) at the same local [26]. If the value of keyhole radius (r_v) is equal to that of incident Gaussian beam radius (r) at ($1/e^2$) of incident intensity, then only (85.5%) of unreflected laser power penetrates the keyhole toward workpiece as the rest dissipates at surface as a heat. As well, at ($1/e$) position of the incident intensity, only 63.2% of laser power enters the workpiece. This definitely causes temperature distribution to disturb as the welding width (b) increases at surface and this does not match keyhole-welding condition.

Maximum efficiency of energy transfer through keyhole (η_{KH}) is about (95%) [18] that can be considered constant if the parameters of welding process such as workpiece velocity, laser beam power, focal position and preheating are varying. Hence, the loss in the incident energy should not exceed 5%. Then:

$$r_v \geq 1.2r \quad \text{at } 1/e^2 \text{ of the incident intensity} \tag{2}$$

Where r is the radius of the incident laser beam and r_v is the radius of the vaporized region.

At low laser power, it is very probable that the condition above does not satisfy, so, preheating leads to increase the efficiency (η_{KH}) by increasing value of (r_v) [16]. This is why the preheating being applied to workpiece in order to increase penetration depth at low laser powers. Welding processes are usually performed using high laser powers. If the parameters of welding process mentioned above vary over a definite range and the condition in Eq. (2) is always satisfied, then preheating of workpiece does not affect the efficiency (η_{KH}).

In this study, we discuss effect of workpiece preheating on some parameters of laser keyhole welding process. We also suppose that the condition of Eq. (2) is already satisfied or approached and the value of efficiency (η_{KH}) is known to be unity.

2. Modeling

The temperature distribution (T_L) along distance (z, $z+dz$) of melted region surrounding the keyhole is given as:

$$T_{L,z}(x,y) - T_{P,z} = \frac{P_z}{4k}\left(\frac{4N}{vx^2}\right)\exp-\left(\frac{v\sqrt{x^2+y^2}}{4N}\right) \tag{3}$$

where T_p is the temperature of bulk region at the edge of the molten pool (liquid phase), P_z is optical power per unit length transferred to the solid, v is welding velocity, N is thermal diffusivity of workpiece material, x is the horizontal coordinate of workpiece movement and y is the half width of the melted region. This equation is valid as the coordinate (z) is localized to welding depth (t), i.e., $0 \leq z \leq t$ and $T_m \leq T_{L,z}(x,y) \leq T_v$, where T_v, T_L and T_m are the vaporization, liquid-phase and melting temperatures, respectively. It can be applied on surface of workpiece according to the following initial boundary condition:

$$T(x=0, y=r_v, z=0) = T_v \tag{4}$$

The Gaussian beam has a circular intensity distribution and Eq. (4) represents an elliptical distribution of temperature given in Eq. (3). This distribution corresponds a circle when $T=T_v$ where $r=\pm x^2+y^2$ and $y=\pm r_v$.

Knowing that [17]

$$T - T_o = \frac{AP_z}{2\pi kv}\frac{1}{\sqrt{t(t+t_o)}}$$

$$\exp-\frac{1}{4N}\left[\frac{(z+z_o)^2}{t} + \frac{y^2}{t+t_o}\right] \tag{5}$$

where A is the absorptance, and

$t_0 = \frac{r_B^2}{4N}$ is heat transfer time and r_B is the Gaussian beam radius at *1/e* of the intensity at surface, and

$$t = \frac{x^2}{4N}$$

we obtain the following expression:

$$T - T_o = \frac{(1-R)P_z}{2\pi kvt}\exp-(\frac{x^2+y^2}{4Nt}) \quad (6)$$

where T_o is the initial temperature of workpiece

Solving at $y=0$, as the workpiece is moved usually in one direction (x), then

$$T - T_o = \frac{(1-R)P_z}{2\pi kx}(\frac{4N}{vx})\exp-(\frac{vx}{4N}) \quad (7)$$

We define the temperature difference in term of laser power entering workpiece through keyhole as:

$$T_v - T_p = \frac{P_{KH}}{2\pi k_L x}(\frac{4N}{vx})\exp-(\frac{vx}{4N}) \quad (8)$$

where k_L is the liquid-phase thermal conductivity of workpiece material and T_p is the temperature of diagnostic probe used for temperature measurement.

When x is too small, then the effect of exponential term is going to be negligible [17], so

$$T_v - T_p = \frac{P_{KH}}{2\pi k_L x}(\frac{4N}{vx}) \quad (9)$$

The laser power transferred to the workpiece includes a part transferred to the whole bulk of solid (P_z) which in turn includes a part (P'_z) transferred exactly inside the workpiece through melted (liquid phase) volume by convection, then both terms can be defined as follows [27-28]:

$$T_m - T_p = \frac{P_z}{k_L} \quad (10a)$$

$$T_m - T_f = \frac{P'_z}{k_S} \quad (10b)$$

where k_S is the solid-phase thermal conductivity of workpiece material and T_f is the temperature at a position far from incidence point.

Hence

$$\frac{T_m - T_p}{T_m - T_f} = \frac{P_z}{P'_z}.\frac{k_S}{k_L} \quad (10c)$$

Returning to Eq. (9), we get

$$T_p = T_v - \frac{P_{KH}}{2\pi k_L x}(\frac{4N}{vx}) \quad (11)$$

Substituting Eq. (10) in Eq. (11), we obtain

$$T_m - T_p = (T_m - T_f)\frac{P_z}{P'_z}.\frac{k_S}{k_L} \quad (12a)$$

$$T_p = T_m - (T_m - T_f)\frac{P_z}{P'_z}.\frac{k_S}{k_L} \quad (12b)$$

Now

$$T_v - \frac{P_{KH}}{2\pi k_L x}(\frac{4N}{vx}) = T_m - (T_m - T_f)(\frac{P_z}{P'_z}.\frac{k_S}{k_L}) \quad (13)$$

Then

$$\frac{T_v}{T_m - T_f} - \frac{P_{KH}}{2\pi k_L x(T_m - T_f)}(\frac{4N}{vx}) = \frac{T_m}{T_m - T_f} - (\frac{P_z}{P'_z}.\frac{k_S}{k_L}) \quad (14)$$

and

$$\frac{T_v - T_m}{T_m - T_f} + \frac{P_z}{P'_z}.\frac{k_S}{k_L} = \frac{P_{KH}}{2\pi k_L x(T_m - T_f)}(\frac{4N}{vx}) \quad (15a)$$

To express the ratio of power transferred to bulk to that transferred inside, we write

$$\frac{P_z}{P'_z} = \frac{k_L}{k_S}\{\frac{T_m - T_v}{T_m - T_f} + \frac{P_{KH}}{2\pi k_L x(T_m - T_f)}(\frac{4N}{vr})\} \quad (15b)$$

where $x=r$.

Defining the vaporization parameter (g_v) and preheating parameter (g_m) as follows:

$$g_v = \frac{T_v}{T_m} \text{ and } g_m = \frac{T_f}{T_m} \quad (16)$$

Eq. (15b) can be rewritten as:

$$\frac{P_z}{P'_z} = \frac{k_L}{k_S}\{\frac{1-g_v}{1-g_m} + \frac{P_{KH}}{2\pi k_L x(1-g_m)}(\frac{4N}{vr})\} \quad (17)$$

and

$$\frac{P_{KH}}{x} = 2\pi k_L(1-g_m)(\frac{4N}{vr})\{\frac{1+g_v}{1-g_m} + \frac{P_z}{P'_z}.\frac{k_S}{k_L}\} \quad (18)$$

In order to solve the last equation, we have considered thermal and physical properties of low-carbon steel and some parameters of laser beam and workpiece supposed to be used in laser keyhole welding. Even though, this treatment is not necessarily valid for all metallic alloys as the treatment is entirely depends on thermal and physical properties of the workpiece material. Table (1) indicates the values of parameters considered in solutions of this treatment.

Table (1) Values of parameters used in this study

Parameter	Value
Melting Temperature	1820°C
Vaporization Temperature	2873°C
Thermal conductivity of solid phase (k_S)	59.5 W/m.K at 0°C
	53.2 W/m.K at 100°C
Thermal conductivity of liquid phase (k_L)	0.5 k_S
Thermal Diffusivity (N)	1.69 x 10^{-5} m^2/s
Laser Power (P)	Up to 3 kW
Laser beam radius (r)	0.05-1 mm
Workpiece velocity (v)	0.05-10 mm/s

3. Results and Discussion

Fig. (2) shows the effect of laser beam radius on the ratio of power transferred to the bulk through keyhole by conduction to that by convection. As shown, this ratio increases with increasing radius (r) but it is limited by the value of radius at which laser beam intensity being low to carry out thermal process required. The optimum case of power transfer to workpiece is

achieved when the laser beam radius is nearly equal to radius of vaporized hole then most power will be coupled to the hole, therefore keeping this condition satisfied by control laser beam radius will then control laser keyhole welding process. Furthermore, radius of vaporized region (r_v) relates to welding width, and then it can be increased by decreasing welding width in order to couple more laser power into workpiece through the keyhole as increasing welding width increases absorption of laser power by liquid phase (molten). Since just the central part of laser beam is supporting the vaporization of material, then increasing absorption by molten decreases beam intensity required for vaporization as well as increase welding width more. Larger vaporized region (deeper depth and wider width) corresponds to faster formation of keyhole. Use of focusing optics is the usual effective method to raise laser beam intensity and reduce its radius despite limitations of such procedure. Both procedures, thermodynamic and optical, can support laser keyhole welding process toward better results.

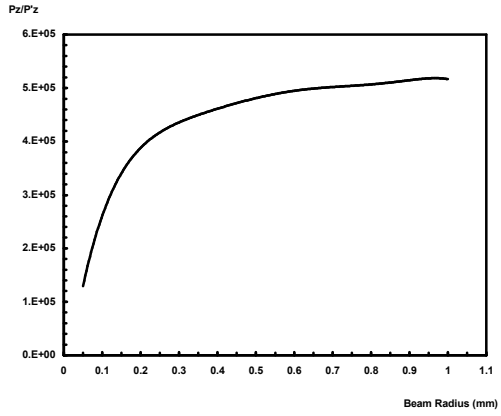

Fig. (2) Effect of laser beam radius on the amount of power transferred to the workpiece through keyhole

If the workpiece is heated by an external source, then the bulk will deliver optical power lesser than the case without heating. The amount being lost due to thermal conductivity of the bulk will now be consumed to heat interaction region more and more. As interaction region is already melted and/or vaporized, then the additional consumed power will support penetration of laser beam inside workpiece to an optimum value of preheating parameter over which whole workpiece would melt. Figures (3) and (4) explain the effect of preheating temperature (T_f) and hence preheating parameter (g_m) on the ratio P_z/P'_z. Depending on properties of laser beam and workpiece considered here, heating workpiece to a temperature near to melting point reduces the high laser power needed for welding depth required as well as time of keyhole formation. This is an assumption and the maximum value of preheating parameter (g_m) does not exceed (0.84) in order not to induce any change in the crystalline structure of the bulk [25, 27]. As shown, initial increasing in preheating temperature leads to rather small increasing in the ratio (P_z/P'_z) as it is limited mainly by thermal conductivity of solid and liquid phases, but at higher temperatures, the ratio (P_z/P'_z) is limited by liquid phase conductivity (k_L) more than that of solid phase (k_S). Also, Fig. (4) confirms the optimum value of preheating parameter (g_m) about (0.84) at which all power transferred to bulk (P_z) is coupled into workpiece.

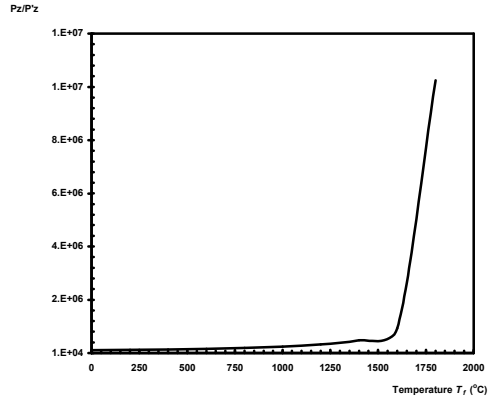

Fig. (3) Effect of preheating temperature on the amount of laser power being transferred to workpiece through keyhole

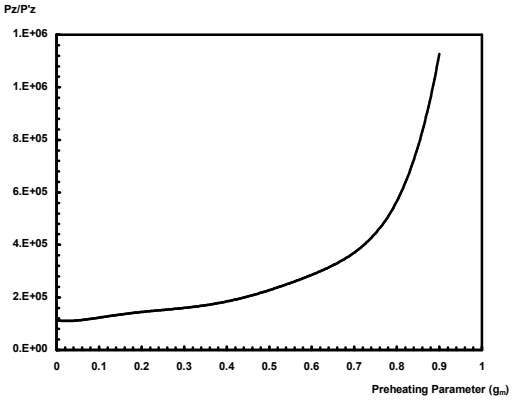

Fig. (4) Effect of preheating temperature on the amount of laser power being transferred to workpiece through keyhole

The term *(vr/4N)* represents a coupling parameter controlling the ratio (P_{KH}/x) by laser beam radius (r) and workpiece velocity (v). Fig. (5) explains variation of P_{KH}/x with coupling parameter *(vr/4N)* at different value of preheating parameter (g_m) and the minimum value of ratio (P_z/P'_z). From this figure, we can determine a range of minimum and maximum values of parameter *(vr/4N)* over which optimum operation can be achieved, as both workpiece velocity and preheating process are practically limited.

Preheating process is applied overall workpiece bulk, which may cause in some cases to deform the structure of solid. So, preheating can be applied to a limited region exactly in front of laser beam incidence by localized-heating techniques at too short times to prevent heat transfer to bulk.

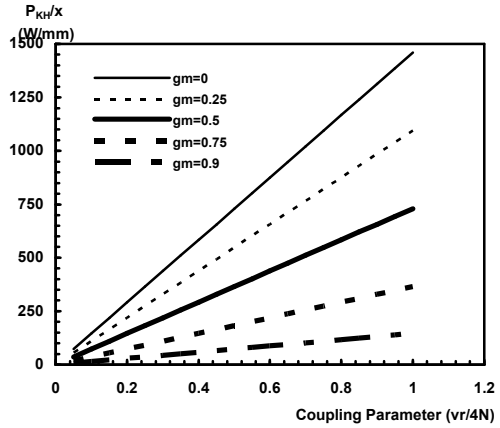

Fig. (5) Variation of laser power per transferred through keyhole per unit length with the coupling parameter (*vr/4N*)

As confirmed, welding process includes several parameters of importance little than laser power such as workpiece velocity (v), laser beam radius (r), thermal diffusivity (N) and preheating parameter (g_m). so, we can introduce the relation between the coupling parameter ($vr/4N$) and preheating parameter (g_m) at the minimum of P_z/P'_z as shown in Fig. (6).

4. Conclusion

Regarding to results presented in this study, it can be stated that the optimum case of power transfer to workpiece is achieved when the laser beam radius is nearly equal to the radius of vaporized hole then most power will be coupled to hole. Therefore keeping this condition satisfied by control laser beam radius will then control laser keyhole welding process. The optical power is transferred to the bulk by conduction is much higher than that transferred by convection. Depending on properties of laser beam and workpiece, preheating the workpiece to a temperature higher than its initial temperature reduces the laser power needed for the required welding depth as well as time of keyhole formation. Both term *(vr/4N)* and preheating effect (T_f/T_m) control the optical power transferred to bulk through keyhole per unit length by controlling laser beam radius (r), workpiece velocity (v) and preheating parameter (g_m). This study is based on the thermal and physical properties of low-carbon steel and may be not suitable for all metallic or steel alloys. This is because the sensitivity of the treatment and its results to such properties.

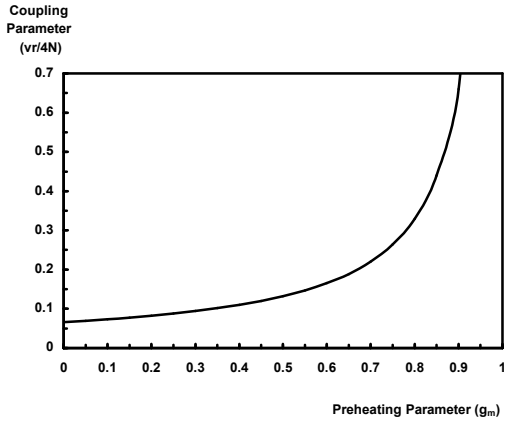

Fig. (6) Variation of coupling parameter (*4N/vr*) with preheating parameter (g_m) at the minimum of (P_z/P'_z)

References

[1] J. Darchuk and L. Migliore, "The Basic of Laser Welding", *Laser & Application*, 59-66 (1985).

[2] D. O'Shea, W. Russell and W. Rades, **"An Introduction to Laser and Their Applications"**, Addison Weasley Publishing Co. (1977) 250-260.

[3] T. Chande and J. Mazumder, *J. Appl. Phys.*, 57(6), 2226-2232 (1985).

[4] M. Bass, **"Laser Material Processing"**, North-Holland Pub. Co. (1983) 155.

[5] M. Sparks, **"Theory of Laser Heating of Solids: Metals"**, *J.Appl.Phys.*, 47, 837-849 (1976).

[6] H. Shercliff and M. Ashby, *Metal. Trans.* 22A(10), 2459-2466 (1991).

[7] H. van Halewijn, **"Laser Material Processing"** in The Industrial Laser Handbook, Springer-Verlag (1992) 108-112.

[8] M. Lax, *J. Appl. Phys.*,48, 3919-3924 (1977).

[9] M. von Allmen and A. Blatter, **"Laser-Beam Interactions with Materials"**, 2nd edition, Springer-Verlag (Berlin) (1995) 68-114.

[10] C. Chon, J. Mazumder and M. Chen, *J. Appl. Phys.*, 64(11), 6166-6174 (1988).

[11] M. Müller and F. Dausinger, "Online Process Monitoring and Control of laser Welding", Int. Body Eng. Conf. & Expos., IBEC'97, Stuttgart, Germany (1997).

[12] V. Babenko and V. Tychinskii, *Sov. J. Quantum Electron.*, 2(5), 399-410 (1973).

[13] S. Na and S. Lee, "Numerical analysis of laser surface hardening of a medium carbon steel", 3rd Int. Conf. on Laser, Paris, France, June 1986.

[14] T. Chande and J. Mazumder, *Metall. Trans.*, 14B, 181-190 (1983).

[15] R. Peretz and H. Mayer, *Optics and Laser in Engineering*, 6, 225-250 (1985).

[16] R. Peretz, *Optics and Lasers in Engineering*, 7, 69-81 (1986).
[17] N. Rykalin, A. Uglov, and A. Kokora, **"Laser Machining and Welding"**, MIR Pub. (Moscow) (1978) 182-199.
[18] R. Willgoss, H. Megaw and J. Clark, *Welding & Metal Fabrication*, March 1997, 117-126.
[19] C. Chan, J. Mazumder and M. Chen, *Metal. Trans.*, 15A, 2175-2184 (1984).
[20] J. Dowden et al., *J. Laser Appl.*, 8, 183-190 (1996).
[21] A. Matsunawaet al., *J. Laser Appl.*, 10, 247-254 (1998).
[22] T. Klein et al., *J. Phys. D: Appl. Phys.*, 27, 481-486 (1994).
[23] T. Klein et al., *J. Phys. D: Appl. Phys.*, 27, 2023-2030 (1994).
[24] T. Forsman, J. Powell and C. Magnusson, *J. Laser Appl.*, 13, 193-198 (2001).
[25] J. Greses, C. Barlow, P. Hilton and W. M. Steen, **"CO_2 and Nd:YAG laser welding process efficiencies"**, University of Cambridge (2002) Private Communications.
[26] P. Fuerschbach and R. Eisler, *J. Mater. Manuf.*, 108, 1-7 (1999).
[27] D. Berglund, **"Simulation of welding and stress relief heat treating"**, Licentiate thesis (2001) Technical Lulea University.
[28] M. Frewin and D. Scott, *Weld. Res. Suppl.*, January 1999, 15-22.

Effects of $CaO–B_2O_3$ Glass on Sintering and Microwave Properties of Cordierite Ceramics for Low-Temperature Cofired

Ahmed M. Jasim *
Hussain J. Hameed

Department of Mechanical Engineering,
College of Engineering,
University of Babil,
Hilla, Babil, IRAQ
** ahmedm80@hotmail.com*

The densification behavior and dielectric properties of cordierite ceramics adding three different proportions of $CaO–B_2O_3$ glass were investigated. The cordierite ceramics were prepared from the waste of porous ceramics. Their crystalline phases, densification parameters, dielectric properties, and microstructure were addressed. The densities of all samples firstly increased and then decreased. The crystalline phase of samples was cordierite. It was considered that $CaO–B_2O_3$ glass and cordierite ceramic did not react in the process of sintering. With 10, 15, 20 wt% $CaO–B_2O_3$ glass added, the maximal densities of samples were 2.46, 2.42, and 2.33 g/cm^3, respectively, obtained at 1060, 1000, and 940°C. The materials had a low dielectric constant and a low dielectric loss [ε~5, tan δ~(2-3) x10^{-3}, at about 10GHz]. The sample, with 15wt% $CaO–B_2O_3$ glass added, sintered at 1020°C (binder burning temperature at 500°C, with a heating rate of 3°C/min) had better properties (ε~5.14, tanδ=2.23x10^{-3} at 10.328 GHz).

Keywords: Cordierite ceramics, $CaO–B_2O_3$ glass, LTCC, Dielectric properties, Sintering
Received: 1 February 2008, Accepted: 15 May 2008

1. Introduction

With the development of high-frequency communication and electronic surface mount technology, the demand for low-dielectric-constant, low-temperature cofired ceramics (LTCC) packaging is increasing. However, most of the microwave dielectric ceramics need a high temperature for sintering [1-2]. To solve this problem, many low-melting temperature glasses are added to ceramics to reduce the sintering temperature [3-5].

As cordierite ceramic has a low dielectric constant (ε~5-6), high resistivity, good thermal and chemical stability, and a low thermal expansion coefficient, it is an alternative material to be used as a substrate substituting for alumina [6-8]. However, cordierite ceramics have a very narrow sintering temperature range and are not easily sintered below 1000°C without any sintering aids; its sintering temperature is about 1500°C. Some sintering aids can improve the sintering ability of cordierite ceramics, but also damage its properties, such as thermal expansion and dielectric constant [9-10].

In this study, the waste materials generated from the process of producing porous cordierite ceramics are chosen as the raw materials for reducing the cost. $CaO–B_2O_3$ (CB) glass, as a new aid, was added to the cordierite waste. The purpose of our work is to learn the densification and dielectric properties of cordierite ceramics with different glass contents under different sintering conditions.

2. Experimental Methods

CB glass with the composition of CaO 45mol%, B_2O_3 55mol%, using $CaCO_3$ and H_3BO_3 as the raw materials, was prepared by melting in a platinum crucible at 1100°C for 1 h, and the glass was quenched in water into fragments, which were then pulverized and screened to become the CB glass powders. The composition of the waste of porous cordierite ceramics is shown in Table (1).

Table (1) Composition of the cordierite ceramics waste (wt%)

	Composition			
	MgO	Al_2O_3	SiO_2	Fe_2O_3
Content	13.63	34.90	49.42	0.11

Three different ratios of glass and cordierite ceramics were mixed; the compositions of samples are listed in Table (2). The mixtures were ball milled for 3 h, then dried at 120°C and granulated with poly(vinyl alcohol) (PVA). The green powders were shaped by uniaxial pressing at 1000kg/cm^2. These samples were sintered at different temperatures, different binder burning

temperatures (400, 450, 500, and 550°C, with a heating rate of 3°C/min) and different heating rates (1, 3, 5, and 8°C/min, with a binder burning temperature of 500°C).

Table (2) Composition of the cordierite ceramics with different amounts of CB glass (wt%)

	Cordierite ceramics	CB glass
CB_{10}	90	10
CB_{15}	85	15
CB_{20}	80	20

Differential thermal analysis (DTA) was carried out in an alumina crucible using Al_2O_3 as the reference material in the NETZSCHSTA429C analyzer, with a heating rate of 10°C/min. Archimedes' method was used to measure the apparent densities. The crystalline phases of samples were identified using a Rigaku RAX-10 diffractometer with a conventional Cu K-radiation system. The surface of sintered samples was observed by scanning electron microscopy (SEM). The microwave dielectric properties of sintered samples were measured in the frequency range of 9-11 GHz using a network analyzer (Agilent HP8363A).

3. Results and Discussion

Fig. 1(a) shows the thermal properties of CB glass. The glass transition temperature (T_g), crystallization temperature (T_c), and melting temperature (T_m) of CB glass were 640, 795, and 970°C, respectively. As the T_g, T_c, and T_m of glass were low, it produced a liquid phase in the densification process to reduce the sintering temperature of samples, which was suitable for LTCC application. From the DTA curve of the cordierite ceramic with different amounts of glass, as shown in Fig. 1(b), no obvious peaks could be observed. This shows that the reaction of cordierite ceramic with CB glass did not occur during the sintering process, with the results observed by Jean and Gupta [11].

Fig. (2) shows the X-ray diffraction (XRD) analysis results for different samples at different sintering temperatures and the intensity of crystalline phases as a function of the amount of CB glass. The crystalline phases of these samples at different sintering temperatures, with different amounts of glass addition, are cordierite phases. The CB glass did not react with cordierite ceramic in the sintering process. The diffraction intensity of cordierite phases decreased a little with increasing amount of CB glass as shown in Fig. 2(c). The diffraction intensity of the cordierite phase was determined by the intensity of the peak located at about 10°.

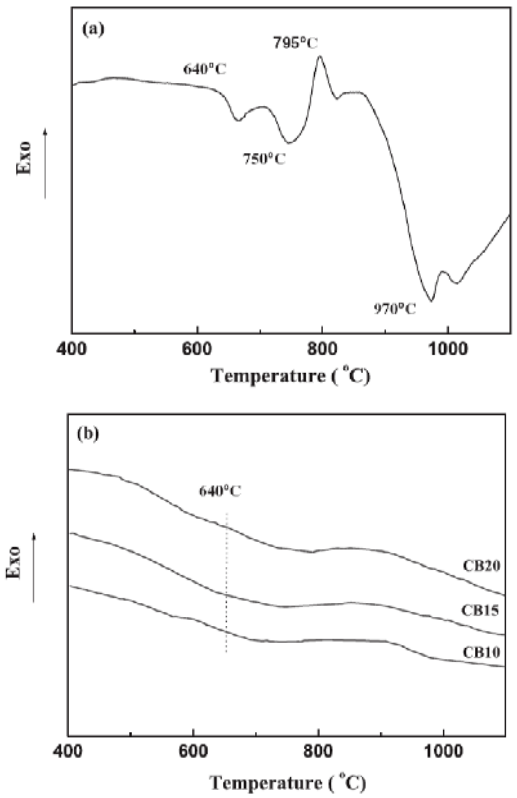

Fig. (1) DTA curves of (a) CB glass and (b) cordierite ceramic with different amounts of glass

Fig. (3) shows s of different compositions of samples sintered at different temperatures for 2h. With increasing sintering temperature, the densities of the samples having the same composition firstly increased and then decreased. From the XRD patterns of samples shown in Fig. (2), CB glass and cordierite ceramics did not react in the sintering process. Therefore, the reason for the variety may be caused by the porosity variation of the samples. The optimal sintering temperature of samples decreased gradually as the CB glass content increased. The maximal densities of CB10, CB15, and CB20 were 2.46, 2.42, and 2.33g/cm^3, at 1060, 1000, and 940°C, respectively. It was considered that CB glass produced a liquid phase in the densification process of the samples and greatly reduced the sintering temperature.

SEM images of samples sintered at different temperatures are shown in Fig. (4). From Figs. 4(a) to 4(d), it can be observed that with increasing sintering temperature, the porosity of CB15 firstly decreased and then increased due to overfiring. From Figs. 4(e), 4(c), and 4(f), it can be found that with increasing amount of CB glass, the optimal sintering temperature decreased from 1060 to 940°C, but the porosity of samples increased. The inner pores of samples did not have enough time to move out of the body with the amount of liquid-phase glass increasing during the sintering process.

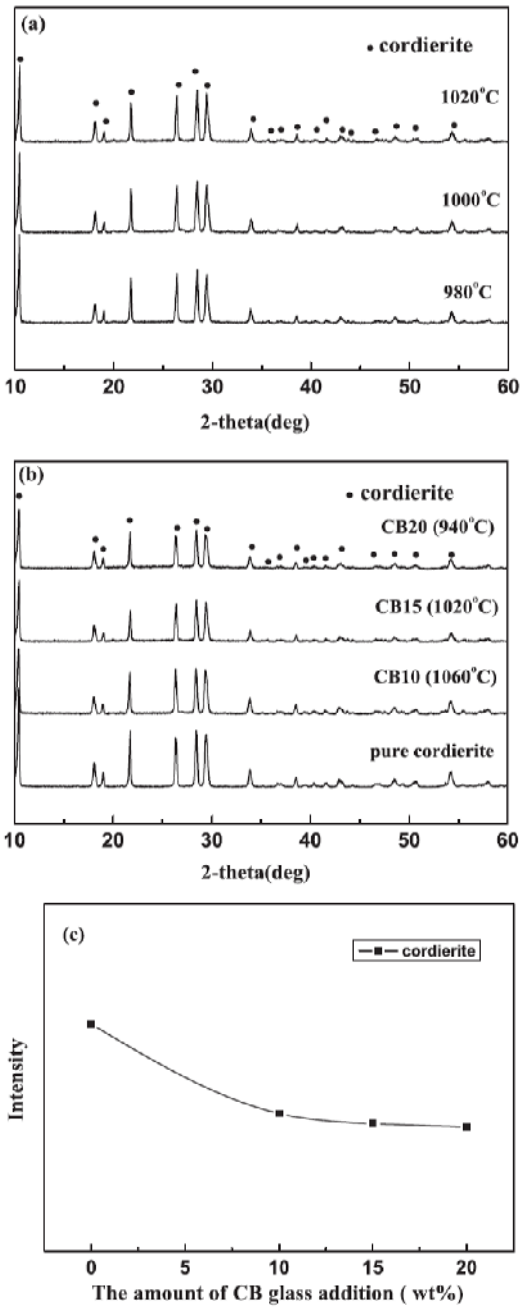

Fig. (2) (a) XRD analysis results for CB15 sample at different sintering temperatures, (b) XRD analysis results for different samples, and (c) diffraction intensity of cordierite phases as a function of the amount of CB glass

Figures (5) and (6) show the dielectric constant and loss of samples with different glass contents as a function of sintering temperature, respectively. The dielectric constants of CB10, CB15, and CB20 firstly increased and then decreased with increasing temperature. The maximal dielectric constants of CB10, CB15, and CB20 were 5.11, 5.14, and 5.06, at the sintering temperatures of 1060, 1000, and 940°C, respectively. The changeable trend was consistent with the patterns of the densities for the investigated samples as shown in Fig. (3).

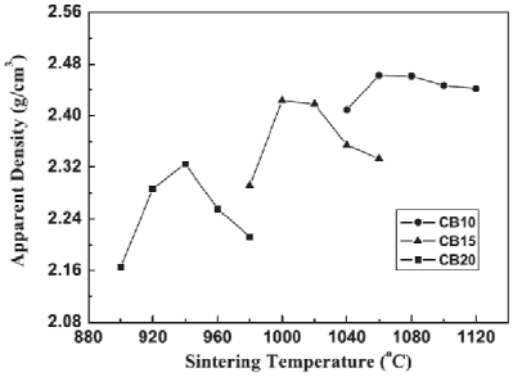

Fig. (3) Apparent densities of the samples as a function of sintering temperature for 2h

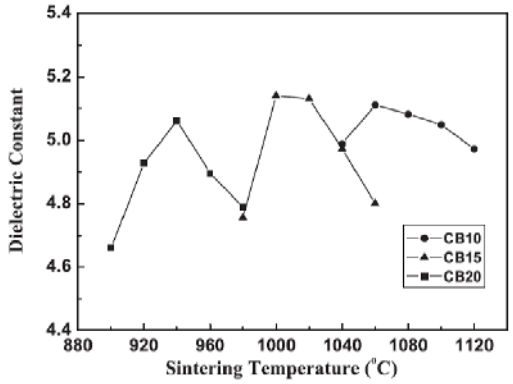

Fig. (5) Dielectric constant of the samples as a function of sintering temperature for 2h

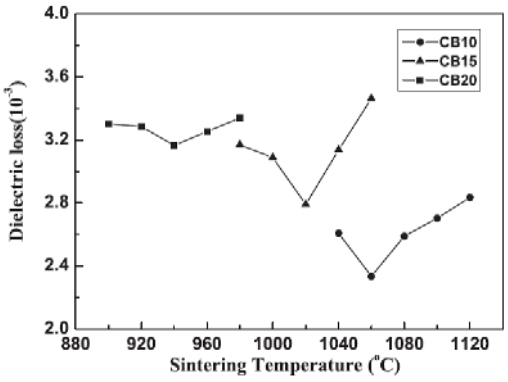

Fig. (6) Dielectric loss of the samples as a function of sintering temperature for 2h

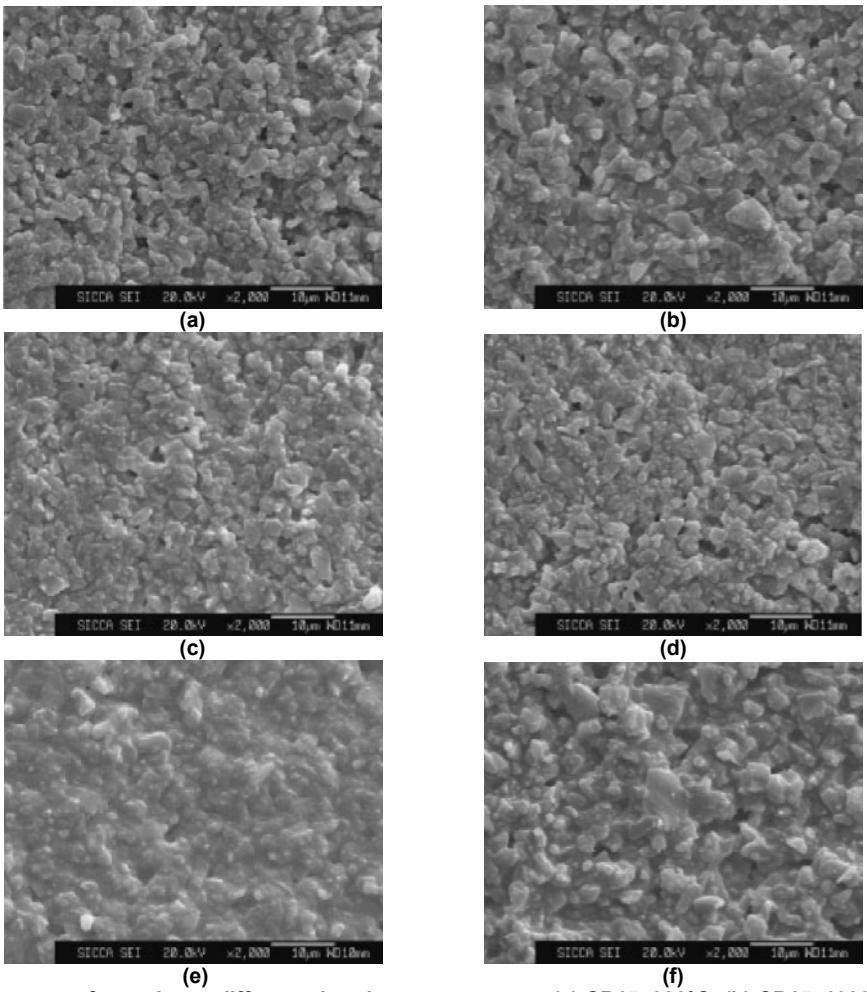

Fig. (4) SEM images of samples at different sintering temperatures: (a) CB15, 980°C; (b) CB15, 1000°C; (c) CB15, 1020°C; (d) CB15, 1040°C; (e) CB10, 1060°C; (f) CB20, 940°C

The same trend was exhibited in the patterns of dielectric loss; the dielectric loss of all samples firstly decreased and then increased. The minimal dielectric losses of CB10, CB15, and CB20 were 2.34×10^{-3}, 2.79×10^{-3}, and 3.17×10^{-3}, obtained at 1060, 1020, and 940°C, respectively. Among all samples, CB15 had better properties, considering both sintering properties and dielectric properties. Thus, CB15 sintered at 1020°C was chosen to investigate the effect of heating rate and binder burning temperature on the properties of materials.

The density, linear shrinkage rate and dielectric properties of CB15 sintered at 1020°C with different heating rate are shown in Table (3). Table (4) shows the properties of the CB15 sample sintered at 1020°C with different binder burning temperatures. It can be obviously observed that the CB15 sample (the binder burning temperature is 500°C, with a heating rate of 3°C/min) had the optimal properties ($\varepsilon \sim 5.14$, $\tan \delta \sim 2.23 \times 10^{-3}$ at 10.328GHz), as a low dielectric constant is required to obtain a higher selfresonance frequency for the materials used for the MLCIs [12].

Table (3) Properties of sample CB_{15} sintered at 1020°C with different heating rates

Heating Rate (°C/min)	Linear Shrinkage Rate (%)	Density (g/cm^3)	Dielectric Constant	Dielectric Loss ($x10^{-3}$)	Measuring Frequency (GHz)
1	17.55	2.44	5.15	2.67	10.446
3	17.35	2.43	5.14	2.23	10.328
5	17.85	2.42	5.13	2.79	9.801
8	17.45	2.43	5.15	2.95	9.933

Table (4) Properties of sample CB_{15} sintered at 1020°C with different binder burning rates

Binder Burning Temperature (°C)	Linear Shrinkage Rate (%)	Density (g/cm^3)	Dielectric Constant	Dielectric Loss ($x10^{-3}$)	Measuring Frequency (GHz)
400	17.55	2.42	5.10	2.92	9.542
450	17.60	2.42	5.11	2.82	9.796
500	17.35	2.43	5.14	2.23	10.328
550	17.65	2.42	5.11	2.55	9.724

4. Conclusions

$CaO–B_2O_3$ glass did not react with cordierite ceramic in the sintering process. The glass produced a liquid phase in the densification process and greatly reduced the sintering temperature of samples. A higher amount of $CaO–B_2O_3$ glass added increased the dielectric loss of samples. With increasing sintering temperature, the densities and dielectric constants of all samples firstly increased and then decreased. The dielectric losses of CB10, CB15, and CB20 reached their lowest values at sintering temperatures of 1060, 1020, and 940°C, respectively. The CB15 sample sintered at 1020°C for 2h (at a binder burning temperature of 500°C, and a heating rate of 3°C/min) had better properties.

References

[1] P.H. Sun et al., *Jpn. J. Appl. Phys.* 37 (1998) 5625.
[2] C.L. Huang et al., *Jpn. J. Appl. Phys.* 39 (2000) 6008.
[3] R.R. Tummala, *J. Am. Ceram. Soc.* 74 (1991) 895.
[4] J.H. Jeana and T.K. Gupta, *IEEE Trans. Component Packag. Manuf. Technol.*, Part B 17 (1994) 228.
[5] Y.J. Seo and J.H. Jung, *J. Am. Ceram. Soc.* 90 (2007) 649.
[6] S.H. Knickerbocker, A.H. Kumar and L.W. Herron, *Am. Ceram. Soc. Bull.* 72 (1993) 90.
[7] G.H. Chen and X.Y. Liu, *J. Alloys Compd.* 431 (2007) 282.
[8] M.A. Subramanian and U. Chowdhry, *Bull. Mater. Sci.* 16 (1993) 665.
[9] M. Awano, H. Takagi and Y. Kuwhara, *J. Am. Ceram. Soc.* 75 (1992) 2535.
[10] R.G. Chandran, K.C. Patil and G.T. Chandrappa, *J. Mater. Sci. Lett.* 14 (1995) 548.
[11] J.H. Jean and T.K. Gupta, *J. Mater. Sci.* 27 (1992) 4967.
[12] Z. X. Yue and J. Zhou: J. Mater. Sci. Lett. 19 (2000) 213.

Nadir F. Habubi [1]
Khudheir A. Mishjil [1]
Hayfa G. Rashid [1]
Bassam G. Rasheed [2*]

[1]*Department of Physics, College of Education, Almustansiriya University, Baghdad, IRAQ*
[2]*School of Applied Sciences, University of Technology, Baghdad, IRAQ*
** bassam_rasheed@yahoo.com*

Computation of Optical Energy Gap of Cu_2O Thin Film: Theoretical Estimation

Thin films of cuprous oxide Cu_2O have been prepared using spray pyrolsis technique. Experimentally, the optical energy gap of Cu_2O was about 2.2eV. To achieve and estimate an accurate E_g value, there was problem in the selection of exact tangent point. To overcome this problem, Newton-Raphson method and mean-value theorem were used. It was found that the mean-value theorem can predict correlated nearly satisfactory E_g value than the other method.

Keywords: Cu_2O films, Spray pyrolsis, Energy gap, Newton-Raphson method
Received: 10 April 2008, Accepted: 25 May 2008

1. Introduction

Determination of the band gap energy of semiconductors and specially semiconductor nanostructures is of great interest since it is directly related to the nanometer sized particles. Therefore, many efforts have been focused on the evaluation of the band gap energy to investigate the optical properties. Semiconductor nanoparticles produced by various methods constituting different sizes, thereby particles size distribution introduces many consequences on the optical properties due to the corresponding band gap. Therefore studying the particle size and their size distribution could be considered a crucial point.

Cuprous oxides Cu_2O and CuO are the main semiconductor phases of copper oxides. Cu_2O form a cubic structure with lattice parameter of 4.27Å [1] and direct band gap of 2.2eV, while CuO has monoclinic crystal structure and indirect band gap of 1.4eV [2]. A metastable copper oxide paramelacouite Cu_4O_3, which is an intermediate compound between the Cu_2O and CuO also been reported [3]. Due to copper oxides potential applications, such as, in solar cells [4], catalysis [5], and magnetic devices [6], much attention has been attracted. Recently, extraordinary efforts have been made to investigate the optical properties of Cu_2O. Mishinia *et al* have studied the structure of Cu/Cu_2O multilayer preparation using nonlinear electrochemical deposition with high precision in control thicknesses and number of layers. Their results lead to significant changes in the linear and nonlinear optical properties of Cu_2O and CuO multilayer structure [7]. Liu *et al* reported the structural and optical properties of films electrodeposited on different substrates. Their results illustrate that, the kind of substrate strongly affect film morphology, crystal structure and optical properties [8]. Prevot *et al* studied the near infrared optical and photoelectric properties of Cu_2O under oxygen atmosphere. The absorption near the fundamental edge was characterized by several absorption bands with peak position at 0.65um, 0.75um, 0.88um, 1.1um with strongest one at 1.28um [9].The aim of this work is to find an appropriate theoretical consideration to obtain the value of the optical energy gap and compare results with experimental values.

2. Experiment

The coatings were deposited on to heated borosilicate glass substrates (Bk-7), aqueous solution containing 2.41gm of $Cu(NO_3)_3.3H_2O$ were used to prepare Cu_2O thin films. The spraying setup and the preparation technique have been described elsewhere [10]. It has found that coatings adherence to substrate were obtained under deposition conditions of substrate temperature T_S=360°C, spraying rate of $10cm^3$/min, air pressure of $10^6 dyne/cm^2$ and distance between nozzle and substrate 28±1.0cm.

The substrate was preheated for 30min before spraying the solution. The period of spraying was about 10s followed by 2min waiting to avoid excessive cooling during spraying process. Weighting method was used to find film thickness, here it is found to be 300nm. With the aid of Pye-Umicom SP-100 sphectrophotometer, the absorption spectrum was recorded within the wavelength region (400-900)nm, knowing that all the prepared samples were done under the same conditions.

3. Results and Discussion

Fig. (1) shows the behavior of absorption coefficient versus photon energy calculated from the equation [11]:

$$\alpha = 2.303(\frac{A}{d}) \quad (1)$$

where α is the absorption coefficient (in cm^{-1}), A the corrected absorbance, and d film thickness (in nm). Fig. (1) illustrates that α rise steeply near the absorption edge and linearly beyond this region. Since $\alpha > 10^{-4} cm^{-1}$, therefore plotting α versus E gives a priory insight of vertical transition at the fundamental absorption edge which is related to the direct energy gap.

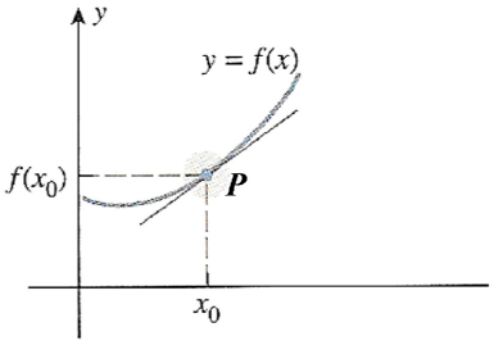

Fig. (1) The behavior of absorption coefficient versus photon energy calculated from equation (1)

The direct energy gap may be found from the relation [12]:

$$\alpha h\nu = B(h\nu - E_g)^{1/2} \quad (2)$$

where B is a constant, E_g energy gap of allowed direct transition and $h\nu$ is the photon energy.

To evaluate the energy gap value E_g many workers used the traditional method, i.e., a plot of $(\alpha h\nu)^2$ versus $(h\nu)$, shown in Fig. (2) [here Matlab [13] and Sigma-plot [14] were used]. This method was based on the fact [15]: "The slope of the curve *y=f(x)* at the point *P=f(x,y)* is defined as the slope of the tangent line to the curve at *P*" as shown.

Therefore, in using this method it's difficult to select the exact tangent point (slope of the graph *y=f(x)* at this point) to achieve an accurate E_g value. This means that the instantaneous rate of change of y with respect to x was evaluated. As a result, an approximated E_g value usually associated with error was obtained. To overcome this problem, we present alternative evaluation methods:

1. Newton-Raphson method (numerical method) [16],
2. Mean-value theorem [15]

The analysis of using these methods was summarized as follows:

Step 1

Using a graphing utility to generate the behavior of experimental data pairs $(\alpha h\nu)^2$ versus $(h\nu)$, shown in Fig. (2). This behavior may be represented in terms of *xy*-plane abbreviation, i.e., *y=f(x)*. Then taking advantage of any general knowledge one have about the function to help in choosing the window.

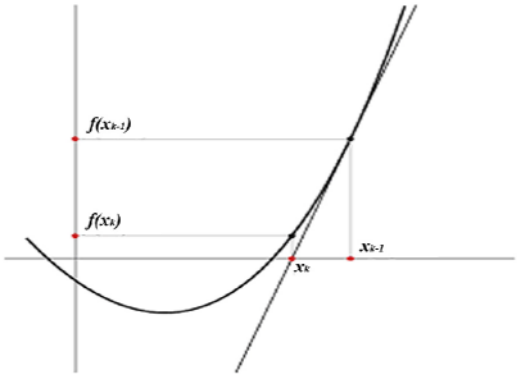

Fig. (2) The behavior of experimental data pairs $(\alpha h\nu)^2$ versus $(h\nu)$

Step 2

Finding the "best fitting" or "good fitting" equation. This may be down with the aid of Matlab or Sigma–plot software package. It is found to be cubic equation yield "best" fitting to experimental data pairs $(\alpha h\nu)^2$ and $(h\nu)$:

Cubic equation: $y = y_0 + ax + bx^2 + cx^3$, where y_0=-0.9891x10^{12}, a=0.2617x10^{12}, b=-1.2150x10^{12}, c=1.8960x10^{12}

Step 3

Finding the "roots", if needed. This may be done using "Matlab" or "advantage plus™" software [17].

Step 4

Calculating first and second derivatives of *y=f(x)* for the cubic equation, this may be done "analytically" or "numerically".

Step 5

Finding the "intercepts", using "Advantage plus™" software, shown in Fig. (3) and the point of intercepts are summarized as follows:

Step 6

Newton-Raphson method:

Usually, this numerical method is used for solving nonlinear algebraic equations. Here, we adapted the basic idea of this method:

- When the real root x_1 is known, then one may easily compute the functional $f(x_1)$. Drawing a line tangent to the curve at point x_1, then the tangent line intersect the x-axis at a point, say x_2, which plays a significant important role in evaluating E_g values, as shown in figure.
- Evaluating intersection point of tangent line with x-axis:

$$x_{K+1} = x_K - \frac{f(x_K)}{f'(x_K)} \quad (3)$$

where, x_{k+1}= approximate root after $k+1$ iterations, x_k= approximate root after k iterations,

$f(x_k)$=functional value at x_k, $f'(x_k)$=first derivative value of the functional at x_k, and $k=1,2,3,...$

As a result, intersection points gives a range of E_g values due to the cases:

a) $f(x)$ and $f''(x)$ [3.5375, 2.8653, 2.4351, 2.1163, 1.8851, 1.6888,…]

b) $f'(x)$ and $f''(x)$ [3.5375, 2.5378, 2.033, 1.7702, 1.615,…]

The *average value* of E_g=2.0746eV, this gives an indication that this method still gives an approximated E_g value.

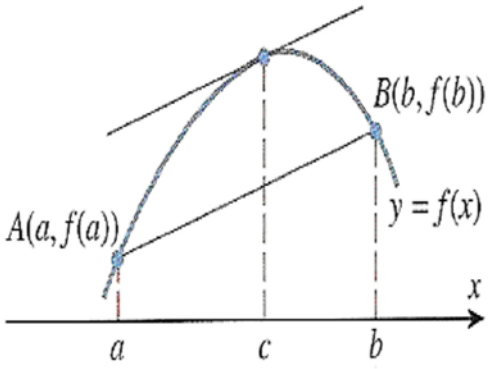

Fig. (3) Finding the "intercepts" using "Advantage plus™" software

Functions	Point of intercept	Decimal Places of accuracy	Number of iterations	Figure
$f(x)$ and $f''(x)$	(1.55089,0.0052) (3.98312,3.8243)	8	4	(3-a)
$f'(x)$ and $f''(x)$	(1.5576,0.0157) (3.5375,3.1246)	8	4	(3-b)

Step 7

Mean-value theorem: This theorem states that "between any points A and B on the graph of a differentiable continuous function $y=f(x)$, there must be at least one place where the tangent line to the curve is parallel to the secant joining A and B" as shown. In this method, the average rate of change of y with respect to x over the interval $[a,b]$ is $\frac{f(b)-f(a)}{b-a}$ equivalent to the slope of the tangent at c, i.e., $f'(c)$. Then E_g values are:

- E_g=2.3674eV, for the case $f(x)$ and $f''(x)$, and
- E_g=2.0370eV, for others

The *average value* of E_g=2.2023eV

From the final result, it is concluded that adapting "mean-value theorem" give results correlate nearly satisfactorily with predicted E_g value [3].

4. Conclusion

From previous results one can conclude that the chemical spray pyrolysis method that has been used to perform the experimental measurements required for this investigation was found to work fairly successfully. As well, E_g value predicted using "mean-value theorem" give good value and fit the experimental results much better and quick than others. It was found that good E_g value may be obtained when the second derivative of the fitting equation considered as a secant line than choosing arbitrary secant. The accuracy of E_g value depends on experimental conditions and deposition technique.

References

[1] D. Chauhan et al., *Bull. Mat. Sci*., 29 (2006) 709.
[2] Z. Gan et al., *J. Phys. D. Appl. Phys*., 37 (2004) 81.
[3] J. Li, G. Vizketlethy, P. Revesz and J. Mayer, *J. Appl. Phys*., 69 (1991) 1020.
[4] A. Rkhshani, *Solid State Electron*., 29 (1986) 7.
[5] K. Borgohain et al., *Phy. Rev. B*, 61 (2002) 11093.
[6] R. Borzi et al., *J. Magn. Mater*., 226-230 (2001) 1513.
[7] D.E. Mishina, K. Nagai, S. Nakabayashi, *Nano. Lett*., 1 (2001) 401.
[8] Y.L. Liu et al., *Semicond. Sci. Technol*., 20 (2005) 44.
[9] B. Prevot, C. Carabatos and M. Sieskind, *physcia status solidi (a)*, 10C21 (2006) 455.
[10] O. Agnikotri et al., *Solid State Commun*., 47 (193) 195.
[11] P.P. Sahay, R.K. Nath and S. Tewari, *Crys. Res. Techol*., 42 (2007) 275.
[12] N. Tigau et al., *J. Optoelectronics Adv. Mater*., 6 (2004) 449.
[13] http://www.mathwork.com
[14] http://www.sigmaplot.com
[15] H. Anton, S.L. Divens, I.C. Davis, **"Calculus"**, 7th edition, John-Wiley & Sons, Inc. (New York) (2002).
[16] W. Al-Khafaji and J.R. Tooly, **"Numerical Methods in Engineering"**, Practice, CBS publishing, Japan Ltd. (1990).
[17] http://www.graphingadvantage.com

Underwater Sensing Characteristics of a ZnO Thin Film Sensor Prepared by Spray Pyrolysis

Ali J. Mohammad

Department of Physics, College of Science, Almustansiriya University, Baghdad, IRAQ

In this work, ZnO thin films were prepared by spray pyrolysis technique to fabricate underwater sensors. Results explained that the preparation conditions affect the sensing characteristics and the attenuation in the underwater environment is dependent of distance from sensing signal source and its frequency. The prepared sensor was tested in a water environment containing crude oil and it exhibited reasonable results to sense the oil amount.

Keywords: Thin film sensors, Zinc oxide films, Underwater sensing
Received: 5 January 2008, Accepted: 10 May 2008

1. Introduction

There are many applications of ferroelectric materials, including the measurement of object distance underwater. For underwater techniques, ultrasonic acoustic sensors have better characteristics than do optical devices. Since ultrasonic waves can transmit the through all materials thought not in a vacuum, they are the best choose for application in the detection of opaque objects, underwater image techniques, and in non-destructive measurement. The measurement technique is easy to perform, and the measurement results are accurate. However, using the same sensors to measure distance underwater, the error in distance measurement is seriously enhanced. In order to measure distances accurately, the operating frequency must be increased and the device structure should be improved. Furthermore, to compete with commercial optical cameras in measuring distances, the measuring distance resolution of acoustic devices must be enhanced. The major improvement is made to use high operating frequencies. Devices should be developed for all distance ranges, including long and short distance measurement. On the other hand, a thin film device is a better choice than a bulk piezeoelectric ceramic sensor for high frequency acoustic devices. In addition, the thin film acoustic devices fabrication is similar to fabrication process of integrated circuits (IC) process, which will be reduce the fabrication cost of these devices [1]. There are different techniques have been adopted for the deposition of piezoelectric thin films, which include electron beam evaporation [2], RF diode sputtering [3-4], ion beam deposition [5-6], RF planar magnetron sputtering [7-9], MOCVD [10-14], ECR [15], laser ablation [16-20], and sol-gel [21-25].

2. Experiment

ZnO films were prepared on glass substrates by a homemade spray pyrolysis system. The different molarities of spray solution (0.3, 0.5, 0.6, 0.7)M of zinc chloride ($ZnCl_2.2H_2O$) were dissolved in distilled water and the solution was carried by the compressed air as a carrier gas then fed into a spray nozzle. The flow rate of solution was 10ml/min flows from a 0.5mm-diameter nozzle at a distance of 25cm to the substrate. The substrate temperature was kept constant at (350°C). The single spraying time was (5s) with different number of sprays. Table (1) indicates the molarity and the corresponding film thickness for the prepared samples.

The ultrasonic testing of the prepared ZnO films was carried out using transmitter/receiver underwater set-up containing of a function generator (B&K precision 3020) and an oscilloscope (KENWOOD CS-1021 20MHz). The amplitude of the incident signal was ($18V_{p.p}$) at frequencies ranging within (0.1-100) kHz. The attenuation coefficient (α) of the ZnO films was studied as a function of distance underwater at different frequencies using the following relation:

$$A = A_0 \exp(-\alpha d) \quad (1)$$

Table (1) preparation conditions of the samples prepared in this work

Sample	Molarity (M)	Film thickness (nm)
#1	0.3	765.1
#2	0.5	939
#3	0.6	1026
#4	0.7	1210

3. Results and Discussion

As shown in Fig. (1), the amplitude of the received signal is varied with the distance between the transmitter and the thin film transducer with a 18V incident signal. In general, the amplitude decreases in all samples due to the attenuation inside the testing medium (water) as the volume of water sample is increased as the distance from the source is increased too. So, this effect is in accordance with Beer-Lamberts law of absorption.

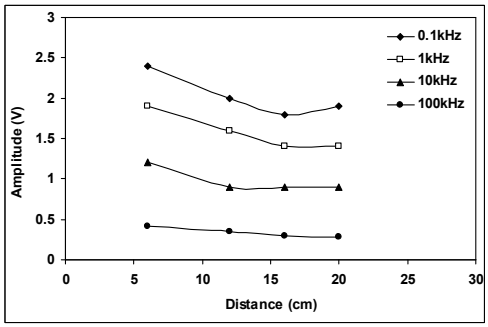

(a) Sample (#1)

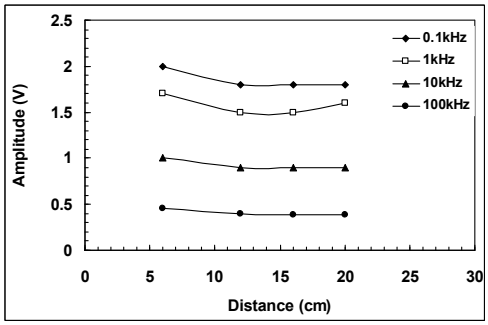

(b) Sample (#2)

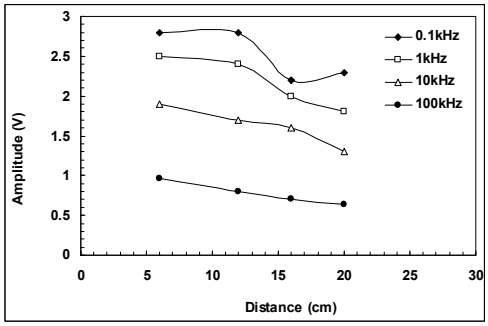

(c) Sample (#3)

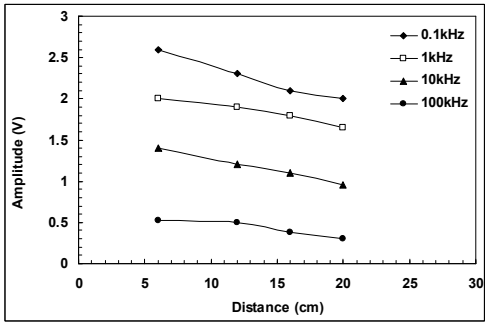

(d) Sample (#4)

Fig. (1) Variation of the underwater received signal with the distance between the transmitter and the thin film transducer at 18V of the incident signal for all samples

Accordingly, Fig. (2) shows the variation of attenuation (αd) by plotting the absorption coefficient (α) versus reciprocal of the distance ($1/d$) for all samples at different frequencies shown in Fig. (1). It is clear that the attenuation increases with increasing distance. Sample (#2) explains higher attenuation at low frequencies (0.1, 1 and 10) kHz but at 100 kHz, sample (#1) explains the higher attenuation. Also, sample (#3) explains the lowest attenuation at all frequencies. Therefore, the attenuation characteristics of such sensor are dependent of the transmitted signal frequency.

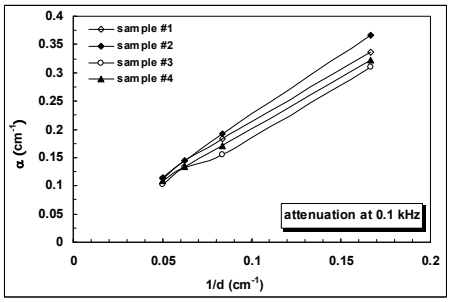

(a) at 0.1 kHz

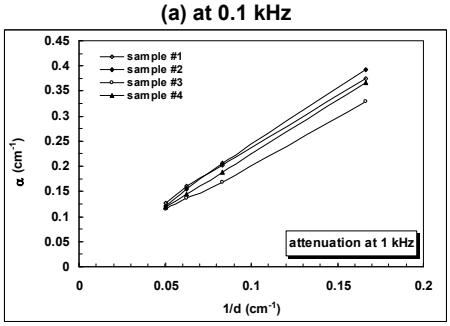

(b) at 1 kHz

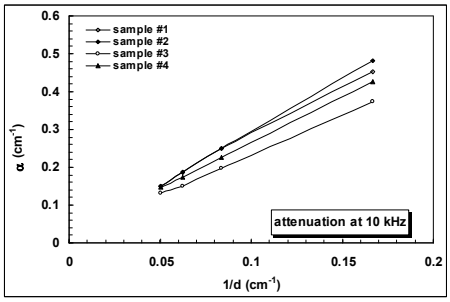

(c) at 10 kHz

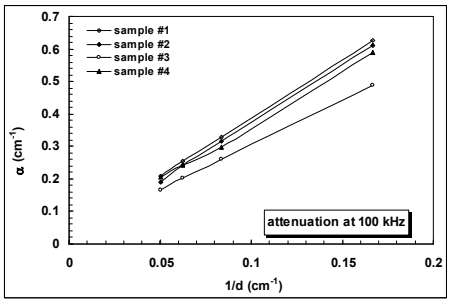

(d) at 100 kHz

Fig. (2) Variation of the attenuation coefficient (α) with the reciprocal of the distance (d) at different frequencies of the incident signal for all samples

The relation between attenuation and frequency is shown more clearly in Fig. (3). The effect of signal frequency can be interpreted as following. The transmitted signal is attenuated by the transmission medium (water) within a period of time, which is the time required by the signal to reach the sensor point. This transmission makes some turbulence in the transmission medium and such turbulence may remain exist over this period of time. When transmission frequency increases, the transmission medium will contain effects of consecutive signals and constructive and destructive interferences would take place. Accordingly, the thin film sensor would receive transmitted signals at a higher frequency and if the sensor needs longer time to distinguish the received signals from each other, then higher frequency may cause destructive interference at the sensor, which in turn affects the final recorded signal amplitude.

If the application requires using such thin film sensors in small samples with high accuracy, then working at small distances (*d*) and low frequencies is the preferred. However, such sensors can be used in case of large samples if the fine accuracy is not very important. Samples of chemicals, medicines and laboratory fluids can be considered as small samples. As well, crude oil pools in seas and drinking water reservoirs are large ones.

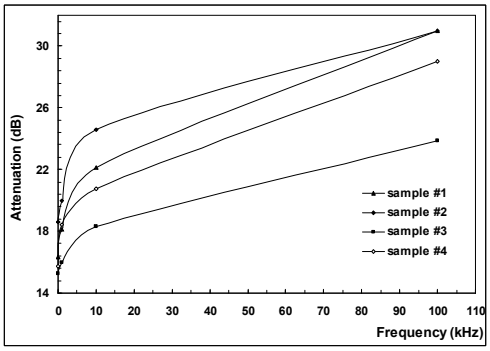

Fig. (3) Relation between attenuation and frequency for all samples

The prepared samples were tested in an environment containing 300ml of water with different amounts of crude oil by transmitting a 18V signal at different frequencies (0.1, 1, 10 and 100) kHz in this environment and recording the amplitude of the received signal at a distance of 8cm and the results are shown in Fig. (4). The amplitude of the received signal was increasing with increasing the amount of oil in the water environment. At lower frequency (0.1 kHz), the maximum signal amplitude was recorded (3.7V) and the amplitude was decreasing as the signal frequency was increased. This is one of the most common applications of the thin film sensors as the sensitivity of such sensors can be optimized by the preparation conditions.

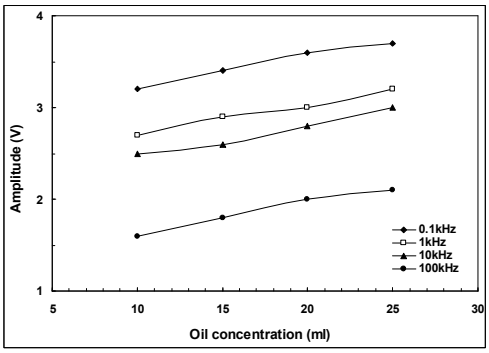

Fig. (4) The sensing characteristics of a 300ml solution of water and crude oil using sample (#3) with a 18V incident signal at distance of 8cm

4. Conclusions

The obtained results explained that the preparation conditions affect the sensing characteristics as the higher molarity used for preparing thin films does not necessarily give the best results. Also, the frequency of the transmitted sensing signal is an important parameter in such method and using low frequencies presented the best results. The attenuation in the underwater environment is dependent of distance from sensing signal source and its frequency. The prepared sensor exhibits reasonable sensing characteristics in a water environment containing crude oil and this would be encourage optimizing the sensor characteristics more in order to improve them in such field of applications.

References

[1] Chang, C.C. and Chen, Y.E., *IEEE Trans. on Ultrasonic, Ferroelectric and Frequency Control*, 1997, 44(3), 624-628.

[2] Oikawa, M. and Toda, K., *Appl. Phys. Lett*., 1976, 29(8), 491-492.

[3] Okada, A., *J. of Appl. Phys*., 1977, 48(7), 2905-2909.

[4] Okada, A., *J. Appl. Phys*., 1978, 49(8), 4495-4499.

[5] Castellano, N. and Feinstein, L.G., *J. Appl. Phys*., 1979, 50(6), 4406-4411.

[6] Pignoleta, W.A. and Levy, F., *Mat. Res. Bull*., 1990, 25, 1495-1501.

[7] Krupanidhi, B., Maffei, N., Sayer, M. and El-Assl, K., *J. Appl. Phys*., 1983, 54(11), 6601-6609.

[8] Takayama, R. and Tomita, Y., *J. Appl. Phys*., 1989, 65(4), 1666-1670.

[9] Sakashita, Y. and Segawa, H., *J. Appl. Phys*., 1993, 73(11), 7857-7863.

[10] Choi, J.H. and Kim, H.G., *J. Appl. Phys*., 1993, 74(10), 6413-6417.

[11] Braun, B., Kwak, S. and Erbil, A. *Appl. Phys. Lett*., 1993, 63(4), 467-469.

[12] Larsen, K.J. et al., *J. Appl. Phys*., 1994, 76(4), 2405-2413.
[13] Peng, C.H. and Desu, S.B., *Appl. Phys. Lett*., 1992, 61(1), 16-18.
[14] Kaub, T.R. et al., *Sensors and Actuators A*, 1994, 45, 125-129.
[15] Auciello, O., *J. Appl. Phys*., 1993, 73(10), 5197-5207.
[16] Frantti, K. and Lantto, V., *J. Appl. Phys*., 1994, 76(4), 2139-2143.
[17] Horwitz, S. et al., *Appl. Phys. Lett*., 1991, 59(13), 1565-1567.
[18] Safari, L.A. and R.L. Pfeffer, *Appl. Phys. Lett*., 1992, 61(4), 1643-1645.
[19] Leuchtner, E. et al., *Appl. Phys. Lett*., 1992, 60(10), 1193-1195.
[20] Yi, G., Wu, Z. and Sayer, M., *J. Appl. Phys*., 1988, 64(5), 2717-2724.
[21] Sanchez, L.E., Wu, S.Y. and Nailk, I.K., *Appl. Phys. Lett*., 1990, 56(24), 2399-2401.
[22] Dey, K., Budd, K.D. and Payne, D.A., *IEEE Trans. Ultrason. Ferroelectr. Freq. Contr*., 1988, 35(1), 80-81.
[23] Amanuma, K., Hase, T. and Miyasaka, Y., *Appl. Phys. Lett*., 1993, 65(24), 3140-3142.
[24] Udayakumar, R.P. et al., *J. Appl. Phys*., 1995, 77(8), 3981-3986.
[25] Kwok, C.K. and Seshu, B.D., *J. Mater. Res*., 1993, 8(2), 339-343.

Abdul-Aziz A. Khalaf *
Majed O. Ghafil
Salah M. Al-Rawi

Department of Physics,
College of Science,
Al-Anbar University,
Al-Anbar Province, IRAQ
** abd_aziz77@yahoo.com*

Study on Compensation of Thermal Stresses in the Fabrication Process of Thin-Film Transistor

It is essential to align masks without tolerance in every deposition step when fabricating thin-film transistors (TFTs) on a polymer substrate. However, the shrinkage of the polymer substrate due to thermal effect may arise during the deposition process. We observed the variation of shrinkage as a function of the annealing temperature. It was found that the substrates keep shrinking up to a critical temperature and stay the same above that point. The thermal treatment was conducted on substrates polycarbonate (PC), the polyarylate (PAR), and poly(ether sulfone) (PES). After predeposition annealing, the shrinkage was prevented but deformation was observed on the surface. An inorganic thin film with a different thermal expansion coefficient was employed to remove the deformation and this resulted in the elimination of strain.

Keywords: Thin film, Shrinkage, Deformation, Misalign, Annealing
Received: 2 March 2008, Accepted: 15 May 2008

1. Introduction

In recent years, flexible display devices such as liquid crystal displays (LCDs) and organic light-emitting diodes (OLEDs) have attracted considerable interest in a wide variety of applications. A polymer substrate is absolutely necessary to realize this type of flexible display devices. Using the polymer as a substrate, numerous advantages including not only mechanical flexibility such as rolling and bending characteristics but also light weight and low cost among others can be obtained. Specifically, the thickness and weight are only one fourth and one half those of a glass substrate, respectively [1-2]. However, it needs low temperature below 150°C in the fabrication process compared with conventional deposition process. The polymer substrate is not as thermally stable as the glass substrate so that some deformation can occur the variation of temperature. In particular, the performance of devices can be easily degraded by the shrinkage of the substrate when it is heated [3-5].

2. Experiment

In this paper, pre-annealing and deposition of the buffer layer described in Table (1) was introduced and studied to solve the previously mentioned problems of shrinkage and the following shear stress [6-11]. In this study, 200-mm-thick polycarbonate (PC) and poly(ether sulfone) (PES) were used as polymer substrate.

The characteristics of each polymer substrate are indicated in Table (2). As it shows, thermal stress, which can cause cracks on the substrate surface, arises due to difference between the coefficient of thermal expansion when heating and cooling.

The plastic substrates were pre-annealed in vacuum to observe thermal stress with the increase as a function of annealing time; 0, 12, 24, 40, 50, 60, 70, and 80 h. As can be seen in Fig. (1), 170-nm-thick Al layer was thermally evaporated and patterned as an alignment to estimate its degree of variation. After annealing with the substrate patterned with the first align key, it was compared with the nontreated substrate with the patterned second align key, which had the same feature as the first one. Subsequently, the dislocation between the two align keys was observed using an Olympus BH3-MJL microscope as shown in Fig. (2). The width and length of the mask keys were on the average 3.83 and 2.85 cm, respectively.

Table (1) Characteristics of buffer layer

Material	Thickness (nm)	CTE (ppm/K)	Dielectric constant	Color
SiO_2	200	1.5	3.9	Transparent

Table (2) Characteristics of polymer substrates

	Tensile Strength (MPa)	Young's Modulus (GPa)	T_g (°C)	CTE (ppm/K)	Dielectric Constant	Color	Chemical	Resistance
							Acetone	Acid
PC	52-72	2.1-2.4	150	70.2	2	Transparent	Bad	Good
PES	83-100	2.4-8.6	228	49.1	3.8	Transparent	Bad	Good
PAR	100	2.9	330	50	2.6	Transparent	Bad	Good
Glass	-	7.3	620	5	5.7	Transparent	Good	Good

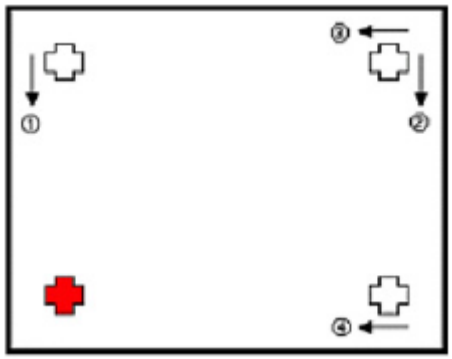

Fig. (1) Structure of align key

Fig. (2) Image of unmatched align key

3. Results and Discussion

In Figs. 3–5, the variation in the shrinkage rate of each polymer substrate is shown for the duration sweep. In figures (3–5), the variation of the shrinkage rates of PC, polyarylate (PAR), and PES is shown up to 80 h annealing time. The difference between pre-annealed and nonannealed substrates becomes smaller as annealing time increases.

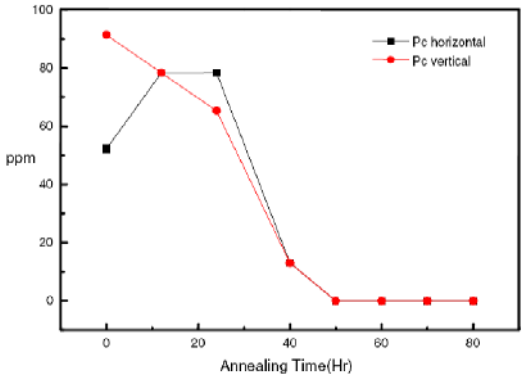

Fig. (3) Shrinkage rate changes of PES substrates as a function of annealing time

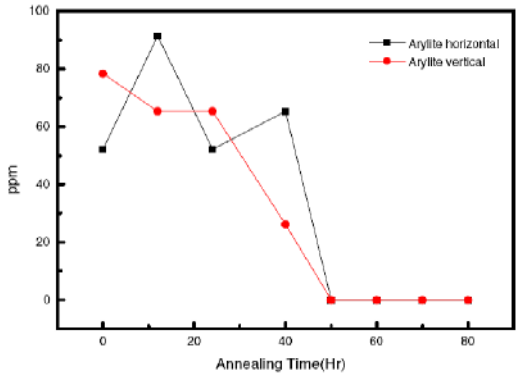

Fig. (4) Shrinkage rate changes of PC substrates as a function of annealing time

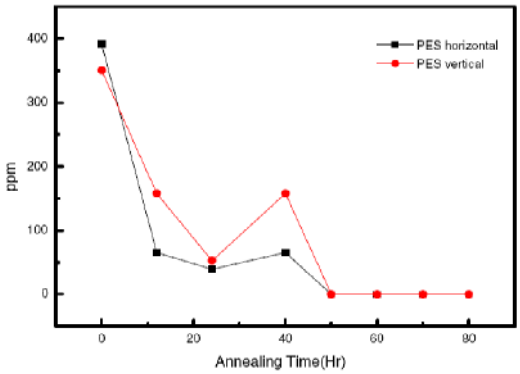

Fig. (5) Shrinkage rate changes of PAR substrates as a function of annealing time

Additionally, it was found that shrinkage of PAR and PES is smaller that of PC. It is assumed that PC has superior thermal endurance compared with the others. PC, PAR, and PES did not shrink after about 48h of annealing not only horizontally but also vertically, which reveals 48h that of pre-annealing is suitable for treatment without shrinkage. Most of the polymer substrates have viscous elasticity so that they cannot be recovered when external energy beyond some threshold is applied. As before, it was found that the substrate was not expanded again after pre-annealing and several subsequent repetitive wet etching processes. Although the shrinkage is reduced by preannealing, strain in the surface can be problematic. Substrate bending was induced by strain in the surface. The equation for strain in the surface is as

$$\varepsilon_{surface} = \frac{t}{2\tau} \qquad (1)$$

where t is the polymer substrate thickness and τ is the radius of curvature. The strain can be considered as another cause of the crack that differs with the strain on the polymer substrate. The strain in the surface can be compensated by the method shown in Fig. (6). It depicts the strain that occurs when two films with different coefficient of thermal expansion are successively deposited. If thin film, which has a different coefficient of thermal expansion with a different coefficient of thermal expansion, is deposited on the other side, the strain expressed in Eq. (2) can compensate the effect of strain from Eq. (1) as

$$\varepsilon_{film} = \frac{h_s + h_f}{2R} \qquad (2)$$

where h_s and h_f are the thicknesses of the substrate and film and R is the radius of curvature. Therefore, if ε_{film} and $\varepsilon_{surface}$ are equivalent, the deformation from strain in the surface can be removed.

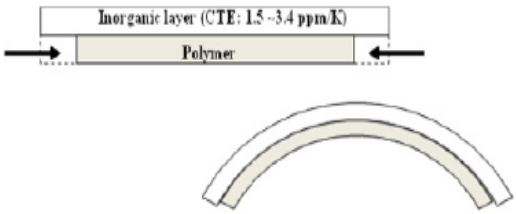

Fig. (7) Effect of inorganic layer on polymer substrate

We have demonstrated that mit controlled shrinkage and strain in the surface are suitable for fabricating devices on a polymer substrate. In particular, the flexible display, which has received a growth of attention, needs to be fabricated on the polymer substrate for thin-film transistor (TFT) applications. The shrinkage of the polymer substrate, the following deformation and strain in the surface in the deposition process can be a cause of error in the fabrication of the TFTs.

4. Conclusion

In this paper, it was revealed that the deformation or errors in different substrates caused by shrinkage and expansion in the wet-etching process can be eliminated by pre-annealing treatment proven by shrinkage test. It was also found that the resultant strain in the surface brought about by the former annealing process can compensated by deposition of buffer layer.

References

[1] Z. Suo and J.W. Hutchinson, *Int. J. Fract.* 43 (1990) 1.
[2] R. Huang et al., *Eng. Fract. Mech.* 70 (2003) 2513.
[3] J.M. Ambrico, E.E. Jones and M.R. Begley, *Int. J. Solids Struct.* 39 (2002) 1443.
[4] K. Kitahara et al., *Jpn. J. Appl. Phys.* 38 (1999) 1312.
[5] J. Malzbender, *J. Appl. Phys.* 95 (2004) 1780.
[6] K. Kitahara et al., *Jpn. J. Appl. Phys.* 41 (2002) 5055.
[7] J.-W. Han et al., *Jpn. J. Appl. Phys.* 45 (2006) 827.
[8] S.-H. Kim et al., *Jpn. J. Appl. Phys.* 44 (2005) 1041.
[9] J.-B. Park et al., *Jpn. J. Appl. Phys.* 43 (2004) 2677.
[10] T.-C. Chen et al., *Jpn. J. Appl. Phys.* 40 (2001) 4087.
[11] Y. Nakano, T. Nomura and T. Takenaka, *Jpn. J. Appl. Phys.* 43 (2004) 5398.

Adawiya J. Haider [1]
Huda M. Hikmet [2*]

[1] *School of Applied Sciences, University of Technology, Baghdad, IRAQ*
[2] *College of Engineering, University of Baghdad, Baghdad, IRAQ*
** hudamh80@yahoo.com*

Characterization of Quantum Well Diode Pumped Nd:YVO_4 Using V-Shape Technique

V-shape face pumping scheme was used, a comparison between the bulk and the QW laser was made when used as pumping sources in CW mode to a Nd:YVO_4 disk crystal, the output power obtained for the bulk diode laser was 29mW, and when using the QW diode laser the maximum output power obtained was 58mW. In pulsed mode when using internally triggered bulk diode laser with prf=1.3kHz, the maximum emitted peak power was found to be 40mW, with a resonator length L=13cm, while for external triggering with prf=3Hz, the maximum output peak power was found to be 145mW.

Keywords: Diode pumping, Nd:YVO_4, Face pumping, Quantum well lasers
Received: 10 May 2008, Accepted: 28 May 2008

1. Introduction

Semiconductor diode lasers, due to the inherently high efficiency of these laser sources (overall optical- electrical efficiencies larger than 60%), are now commonly used (diode laser pumping). Quantum well (QW) lasers are attractive for research because they are both physically very interesting and technologically important. QW technology allows the crystal grower for the first time to control the range, depth, and the arrangement of the quantum mechanical potential wells. In the last decade, the importance of the quantum well laser has steadily grown until today it is preferred for most semiconductor laser applications [1].

Their growing popularity is because, in almost every respect, the quantum well laser is somewhat better than conventional lasers with bulk active layers. One obvious advantage is the ability to vary the lasing wavelength merely by changing the width of the quantum of the QW. A more fundamental advantage is that the QW lasers delivers more gain per injected carrier than conventional lasers, which results in lower threshold currents, [1-3].

The disk lasers are characterized in that the light is amplified passing through a thin disk active layer [2,4]. Such lasers are under intensive research for both pulsed and continuous- wave operation. Such geometry allows the efficient heat sink at small distortions of the wavefront, therefore the scalability to high power is expected, the purpose of face- pumped disk amplifiers is to provide a uniform gain distribution over a very large cross- section. The majority of modern solid-state lasers use neodymium (Nd) doped materials such as Nd:YAG (Yttrium Aluminum Garnet which is $Y_3Al_5O_{12}$), Nd:YVO4, Nd:Glass, and others. The general limit of power scaling comes from the overheating, the surface loss and the amplified spontaneous emission (ASE), [1]. With the geometry of a thin disk for the laser active medium, the ratio of the cooling surface to pumped volume is increased compared to rod lasers, which is a basic advantage to extract high output power from a small volume, [5-6]. The thin disk laser concept is a laser design for diode-pumped solid- state lasers, which allows the realization of lasers with high output power, having very good efficiency and also excellent beam quality, [7-8].

2. Experimental work

The 4x5x0.5mm^3 Nd:YVO_4 crystal, which is AR coated for the wavelength of the pump and laser radiation at the front side and HR coated for both wavelengths at the back side. This crystal was placed on Al plate from its front surface and this plate contains a hole of diameter of 4mm at its centre to permit the radiation comes from the pumping source to incident on the crystal, this hole makes the crystal acts like a disk, also a Cu plate is on its back surface with indium material of 0.1mm thickness as a thermal adhesive, those plates serves as heat sink.

The ray direction for V-shape face pumping, was illustrated in Fig. (1), where the disk crystal and the output coupler mirror were placed at 45°, and the bulk diode laser were used as a pumping source once in CW mode and once in pulsed mode with internal and external triggering, while the QW diode laser was used as a pumping source in CW mode. Proper focusing lenses were used with the two pumping sources to focus the highly diverging beam from these sources.

Two 808nm GaAlAs diode lasers (in bulk (2W) and QW (1W) designs) were used as the

pumping source for such pumping scheme with the ability of CW and pulsed mode operation for bulk source.

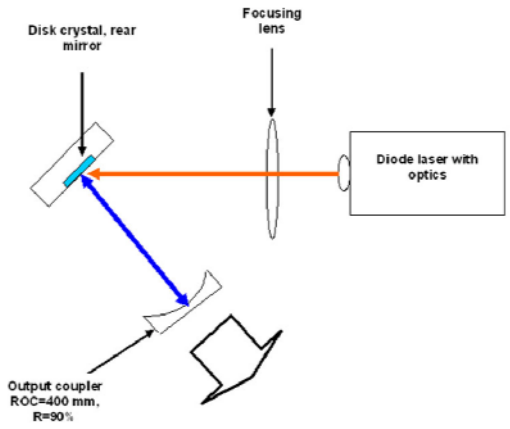

Fig. (1) The ray direction of the V-shape face pumping

3. Results and Discussion

3.1 CW operation

Using the pumping configuration that is proposed for V-shape laser, see Fig. (1), once the pumping source used was the 808nm bulk diode laser operating in CW mode and also the 810nm QW GaAlAs diode laser was also used.

Using the bulk diode laser, Fig. (2) shows a graph between the operating current and the transmitted power from the focusing lens with f=6cm, from this curve the measured radiation transfer efficiency was found to be η_r=53%, the second curve was drawn between the operating current and the radiation emitted from the disk medium, from this curve the measured value for the both the upper state efficiency and the absorption efficiency was found to be $\eta_u\eta_a$=7%.

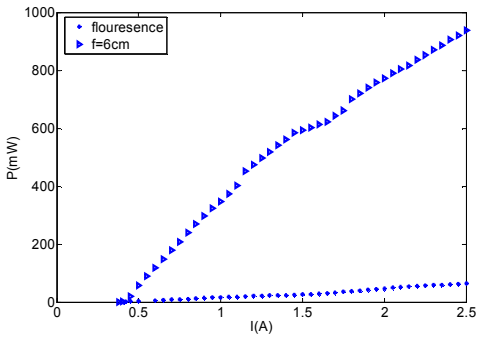

Fig. (2) The operating current vs. the transmitted power

Fig. (3) shows the relation between the operating current of the bulk diode laser and the 1064nm CW laser output power at resonator length of L=13 cm. From this graph it was found that the maximum output power obtained was 29mW, the measured optical to optical slop efficiency $\eta_{o\text{-}o}$=1.7%, and the measured threshold power P_{th} was found to be ≈25mW.

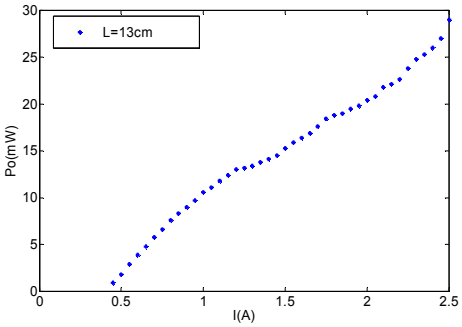

Fig. (3) The current vs. the laser output power at L=13 cm

Now using the QW diode laser as a pumping source instead of the bulk one, two focusing lenses of focal lengths f=(6,3) cm were used to focus the rhombic spot of the QW diode laser onto circular spot of d=4mm in order to occupy the whole face of the disk which is allowed to be pumped, the relation between the pumping power and the transmitted power was shown in Fig. (4). From this graph the radiation transfer efficiency measured was found to be ≈67%, while the fluorescence curve was drawn between the operating current of the QW diode laser and the power emitted from the disk medium and the measured efficiency was found to be $\eta_u\eta_a$=7%.

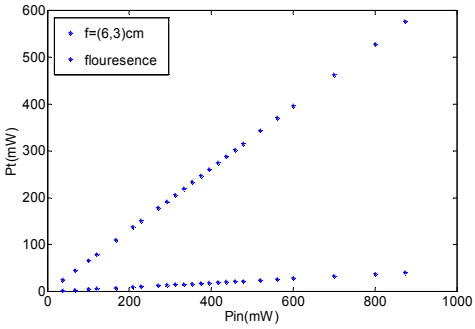

Fig. (4) The pumping power vs. the transmitted power

The relation between the pumping power from the QW diode laser and the obtained 1064nm laser output power using an output coupler of R=90% with different resonator lengths was shown in Fig. (5). It was found that the maximum output power obtained at L=14.5cm and the measured threshold power was found to be P_{th}=37mW, the maximum output power obtained from this configuration was found to be ~58mW, from this curve the maximum measured optical to optical slope efficiency was found to be ≈7% which is higher than that of the bulk diode laser.

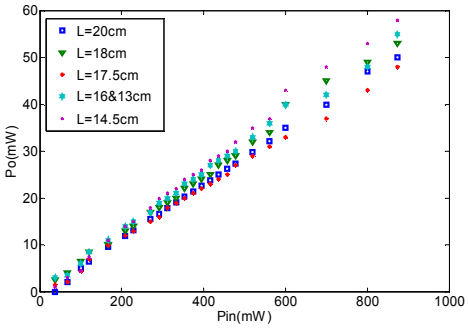

Fig. (5) The pumping power vs. the laser output power at different resonator lengths

3.2 Pulsed operation

3.2.1 Internal triggering

In pulsed operation the internally triggered bulk diode laser was used as the pumping source with a repetition rate of 1.3kHz, the influence of the laser diode operating temperature on the laser output power was investigated as shown in Fig. (6). There is a compromise between the operating temperature T, the input peak power P_{in}, and the output laser peak power P_o, it was found that the maximum output peak power was obtained at T=16°C, the measured threshold peak powers were found to be P_{th}≈713mW, 690mW, 665mW, for operating temperatures of T=20, 18, 16°C respectively, i.e. the measured threshold peak power is increased with increasing the operating temperature of the diode laser at a fixed resonator length of L=13cm, from these values the maximum optical to optical slope efficiency $\eta_{o\text{-}o}$ was approximately equal to 1%.

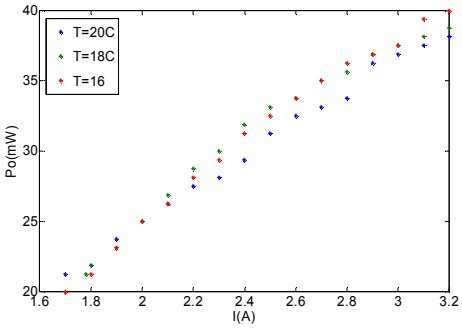

Fig. (6) The current vs. the laser output power at L=13cm.

3.2.2 External triggering

Now the bulk diode laser is externally triggered at different repetition rates (<1kHz) in order to increase the pumping peak power emitted from this source and hence the output laser peak power, the influence of such change was investigated as shown in the following figures.

The focusing lens used was the same as that for internal triggering, so the transmitted peak power from this lens was found to be as shown in Fig. (7), a graph between the operating current of the bulk diode laser at prf=100Hz, the measured radiation transfer efficiency was found to be η_r=52%, it is obvious that the value of this efficiency is low because the lens used in the system was not anti-reflection coated at 808 nm, so a large amount of the pumped beam is lost due to reflection.

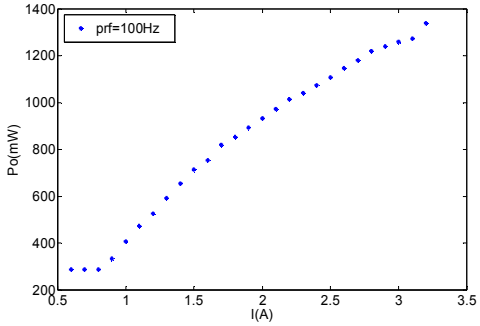

Fig. (7) The current vs. the transmitted pumping peak power

The influence of changing the repetition rate of the pumping source on the 1064nm laser output peak power was investigated at resonator length of L=13 cm as shown in Fig. (8). From this figure the curves were drawn between the pumping current of the bulk diode laser and the 1064 nm laser output peak power with different repetition rates (3-500)Hz, it was found that the maximum output peak power was obtained at repetition rate of 3Hz which was 155mW, and decreases with increasing repetition rate, due to the fact that decreasing the repetition rate will increase the value of the pumping peak power. Also the measured threshold peak power was increased with increasing repetition rate which was P_{th}=670mW to 1882mW for repetition rates of 3Hz to 500Hz, due to the fact that increasing the repetition rate will constrain the internal amplification inside the active medium.

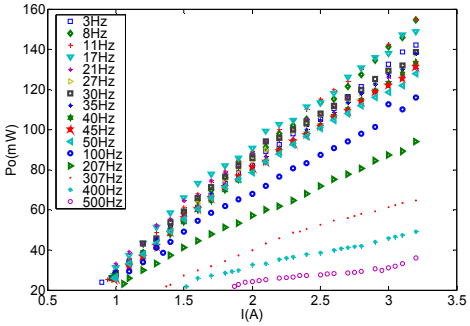

Fig. (8) The current vs. the laser output peak power at different repetition rates, using L=13cm

The maximum optical to optical slope efficiency obtained for this pumping configuration was found to be 7% to 4.3% for repetition rates of 3Hz to 500Hz.

4. Conclusions

From the experimental work it was found that in CW operation of face pumped V-shape laser using QW laser source is more efficient than using bulk diode laser. In pulsed mode it was found that reducing the repetition rate increases the peak pumping power i.e. increases the output laser peak power due to the fact that reducing the temperature of the laser medium and increasing the ability of internal amplification at low repetition rates. It is necessary to use external triggering to lower the repetition rate of the diode laser, which in turn will need less cooling than operating in high repetition rates and will increase the optical to optical slope efficiency of the system due to the increased peak pumping power.

Acknowledgement

Special thanks to Dr. M.K. Al-Ani for his assistance in the accomplishment of the experimental work.

References

[1] W. Koechner, **"Solid-State Laser Engineering"**, 6th ed., Springer Series, 2006.

[2] D. Kouznetsov *et. al.*, *J. Opt. Soc. Am.* B 22(4), 2006.

[3] E. Schiehlen, M. Riedl, "Annual report optoelectronics department", University of Ylm, 2002.

[4] A. Giesen, "Thin disk lasers power scalability and beam quality", LTJ, 42(2), June, 2005.

[5] D. Kouznetsov, *et. al.*, *J. Opt. Soc. Am.* B 23(6), 2006.

[6] C. Stewen, *et. al.*, *IEEE J. of Sel. Topics in Quantum Electron.*, 6(4), July/August 2000.

[7] P.S. Zory, **"Quantum Well Lasers"**, 1993, Academic Press, Inc.

[8] R. Wilhelm, *et. al.*, *IEEE J. Quantum Electron.*, QE-44(1), March 2008.

THE IRAQI JOURNAL OF APPLIED PHYSICS LETTERS
EDITORIAL BOARD

IJAPLett

COPYRIGHT RELEASE

Iraqi Journal of Applied Physics Letters (IJAPLett)

We, the undersigned, the author/authors of the article titled

……

……

……

……

that is presented to the Iraqi Journal of Applied Physics Letters (IJAPLett) for publication, declare that we have neither taken part or full text from any published work by others, nor presented or published it elsewhere in any other journal. We also declare transferring copyrights and conduct of this article to the Iraqi Journal of Applied Physics Letters (IJAPLett) after accepting it for publication. The authors will keep the following rights:

1. Possession of the article such as patent rights.
2. Free of charge use of the article or part of it in any future work by the authors such as books and lecture notes without referring to the IJAPLett.
3. Republishing the article for any personal purposes of the authors after taking journal permission.

To be signed by all authors:

Signature:……..date: ……..

Printed name: ……..

Signature:……..date: ……..

Printed name: ……..

Signature:……..date: ……..

Printed name: ……..

Correspondence address:

……

……

Telephone:……Fax:……..email: ……

Note: Please complete and sign this form and mail it to the below address with your manuscript

The Iraqi Journal of Applied Physics Letters,
P. O. Box 55259, Baghdad 12001, IRAQ
Email: ijaplett.editor@hotmail.com
Mobile: +964-7901274190

CONTENTS

Characterization of D.C. Sputtering System	Ali M. Mousa Adawiya J. Haider Ahmed S. Jabbar	3-9
Modeling of the Preheating Effect on Keyhole Laser Welding Efficiency	Oday A. Hamadi Khawla S. Khashan	10-15
Effects of $CaO–B_2O_3$ Glass on Sintering and Microwave Properties of Cordierite Ceramics for Low-Temperature Cofired	Ahmed M. Jasim Hussain J. Hameed	16-20
Computation of Optical Energy Gap of Cu_2O Thin Film: Theoretical Estimation	Nadir F. Habubi Khudheir A. Mishjil Hayfa G. Rashid Bassam G. Rasheed	21-23
Underwater Sensing Characteristics of a ZnO Thin Film Sensor Prepared by Spray Pyrolysis	Ali J. Mohammad	24-27
Study on Compensation of Thermal Stresses in the Fabrication Process of Thin-Film Transistor	Abdul-Aziz A. Khalaf Majed O. Ghafil Salah M. Al-Rawi	28-30
Characterization of Quantum Well Diode Pumped Nd:YVO_4 Using V-Shape Technique	Adawiya J. Haider Huda M. Hikmet	31-34